Sound generation mechanism of compressible vortex reconnection

Hamid Daryan[1,†], **Fazle Hussain**[2] **and Jean-Pierre Hickey**[1]

[1]Department of Mechanical and Mechatronics Engineering, University of Waterloo, Waterloo, ON N2L 3G1, Canada

[2]Department of Mechanical Engineering, Texas Tech University, Lubbock, TX 79409, USA

We study the sound generation mechanism of initially subsonic viscous vortex reconnection at vortex Reynolds number Re ($\equiv$ circulation/kinematic viscosity) $= 1500$ through decomposition of Lighthill's acoustic source term. The Laplacian of the kinetic energy, flexion product, enstrophy and deviation from the isentropic condition provide the dominant contributions to the acoustic source term. The overall (all time) extrema of the total source term and its dominant hydrodynamic components scale linearly with the reference Mach number M_o; the deviation from the isentropic condition shows a quadratic scaling. The significant sound arising from the flexion product occurs due to the coiling and uncoiling of the twisted vortex filaments wrapping around the bridges, when a rapid strain is induced on the filaments by the repulsion of the bridges. The spatial distributions of the various acoustic source terms reveal the importance of mutual cancellations among most of the terms; this also highlights the importance of symmetry breaking in the sound generation during reconnection. Compressibility acts to delay the start of the sequence of reconnection events, as long as shocklets, if formed, are sufficiently weak to not affect the reconnection. The delayed onset has direct ramifications for the sound generation by enhancing the velocity of the entrained jet between the vortices and increasing the spatial gradients of the acoustic source terms. Consistent with the near-field pressure, the overall maximum instantaneous sound pressure level in the far field has a quadratic dependence on M_o. Thus, reconnection becomes an even more dominant sound-generating event at higher M_o.

Key words: hydrodynamic noise, aeroacoustics

† Email address for correspondence: h42moham@uwaterloo.ca

1. Introduction

The mechanism of aeroacoustic noise production and its relation to the far-field sound propagation remain poorly understood, in spite of decades of dedicated theoretical, numerical and experimental studies. Intuitively, we know that coherent vortical structures and their self- and mutual interactions are significant aeroacoustic noise sources as they are the sinews and muscles of turbulence. In fact, coherent structures and their interactions have been often implicated as the main hydrodynamic source of jet noise (Hussain 1983; Guj *et al.* 2003; Coiffet *et al.* 2006); however, the extent to which coherent structures are important in sound generation (Bastin, Lafon & Candel 1997) and the types of vortical interactions that generate noise are poorly understood.

The idea that aeroacoustic noise can be modulated through the control of vortical structures has inspired many studies. Extending his earlier work (Zaman & Hussain 1981) on jet turbulence suppression, Zaman (1985) investigated noise suppression and enhancement of a subsonic jet through controlled excitation of the vortical structures (see also Hussain & Hasan 1985). A higher level of organization and mutual interaction among the vortical structures in a laminar jet results in higher noise. However, controlled excitation of a transitional low-speed jet can suppress growth rate of the near-exit shear layer's Kelvin–Helmholtz instability and produce weaker coherent structures downstream, thus less noise. These experiments implied that not only the type, but the intensity of the vortical interaction is influential in sound generation. Eldredge (2007) used direct numerical simulation to investigate the sound generation of two-dimensional leapfrogging vortices. He showed that the primary acoustic pulse does not originate from the elastic deformation of the inner vortex cores but from the filamentary structures at the outer edges which rotate about the cores – based on Möhring's analogy (Möhring 1978), vorticity stretching and acceleration emerge as an intense noise source. Eldredge deduced that the sound is not necessarily caused by the explicit collision of the vortex cores.

A consensus on the dominant jet noise generation mechanism emerged in early studies (Williams & Kempton 1978; Kibens 1980; Crighton 1981; Laufer & Yen 1983), where acoustic sources were attributed to vortex pairing. Hussain & Zaman (1981) studied the coherent structures in the near field of an axisymmetric free jet and argued, however, that pairing is completed within four diameters from the jet exit, while most noise originates farther downstream. They proposed that reconnection of the toroidal rings through the evolution of azimuthal lobe structures produces most of the jet noise. Starting with the first suggestion by Melander & Hussain (1988), vortical reconnection, which results in a violent topological change of the vortex tubes, has long been hypothesized as a significant contributor to aeroacoustic noise generation in broader classes of turbulent flows. Figure 1 shows the main stages of the reconnection process of two anti-parallel vortices including inviscid induction, bridging, repulsion of bridges and threading. Given vorticity tilting, i.e. rotation of vorticity vector from the axial direction towards the lateral direction (see figure 1*b*), and the rapid repulsion of the bridges (see figure 1*c*), originating from the self-induced recoil of accumulated reconnected, cusped vortex lines, reconnection could indeed be a significant sound-generating event which has not been adequately explored. For a detailed explanation of the reconnection process, the reader is referred to Melander & Hussain (1988).

In spite of the recent advances in characterizing incompressible reconnection (Hussain & Duraisamy 2011; Yao & Hussain 2020), relatively little is known about the compressible case, which involves a more complicated evolution owing to the strong dependence on the initial thermodynamic conditions (Virk & Hussain 1993) and additional vorticity generation mechanisms through dilatation and baroclinicity (Virk, Hussain &
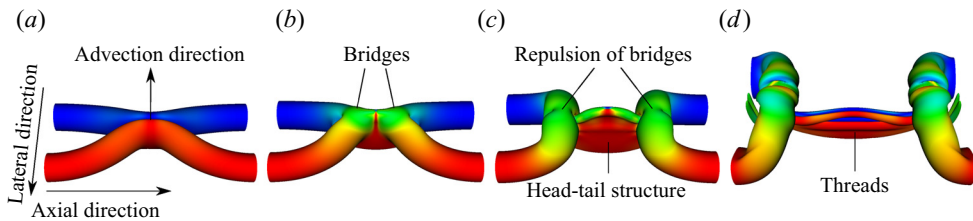
Figure 1. Reconnection process of two anti-parallel vortices including (*a*) inviscid induction, (*b*) bridging, (*c*) repulsion of bridges and (*d*) threading. Blue, green and red colours show negative, zero and positive axial vorticity, respectively.

Kerr 1995). Presumably for these reasons, only a few works have considered compressible reconnection (Kerr, Virk & Hussain 1989; Virk *et al.* 1995; Scheidegger 1998; Shivamoggi 2006; Peng & Yang 2018) – all of which are limited to low *Re*. In the transonic and supersonic regimes, incipient shocklet-induced reconnection alters the vorticity field causing earlier bridging but subsequent slowdown of the circulation transfer. Therefore, at the same *Re*, the time scale of the compressible reconnection increases compared to the incompressible case (Virk *et al.* 1995). It is known that compressibility also affects the domain of influence of vortical structures impacting the level of turbulence anisotropy in canonical flows (Pantano & Sarkar 2002; Hickey, Hussain & Wu 2016). In addition to the hydrodynamic effects, shocklet formation during reconnection could represent an additional aeroacoustic sound source.

Sound generation has been noted in the oblique collisions of vortex rings; the primary acoustic source originates from the reconnection region of vortex lines (Kambe, Minota & Takaoka 1993; Adachi, Ishh & Kambe 1997; Ishii, Adachi & Kambe 1998). Furthermore, Nakashima (2008) showed that as the collision angle decreases, reconnection and its contribution to the far-field sound intensify. On the other hand, using Lighthill's analogy (Lighthill 1952), Scheidegger (1998) failed to find a distinct far-field sound signal during the reconnection of orthogonal vortices. He noted that many source points in the reconnection region contribute to sound generation and the sound radiation is sporadic. Recently, we showed that the reconnection of two anti-parallel vortices produces significant far-field sound which is deterministic in the sound directivity pattern (Daryan, Hussain & Hickey 2020). Our analysis shows that the main acoustic sources are located at the contact region of the vortices at the start of the reconnection and then migrate towards the bridges. In addition to viscous flow cases, sound generation during quantum vortex reconnection becomes an appealing topic, recently identified as an energy exchange and irreversibility mechanism (Proment & Krstulovic 2020; Villois, Proment & Krstulovic 2020).

Although vorticity evolution is qualitatively the same for all subsonic reconnections (Daryan, Hussain & Hickey 2019), many aspects of compressible reconnection including the detailed roles of the supplementary vorticity generation terms, sound production mechanism and recognition and evolution of the dominant components of the acoustic source term still remain unexplored. Also, very little is known about the formation and features of shocklets near the sonic threshold and their dependence on *Re*.

In this paper, we aim to characterize the sound generation mechanism of compressible, viscous vortex reconnection, which is conjectured to play a central role in aeroacoustic noise generation in vortical flows. Our focus is on the dominant components of the acoustic source term, their physical representation and the role of compressibility. We also study the near-field pressure evolution which is closely tied to the sound production and propagation

mechanisms (Coiffet *et al.* 2006; Mancinelli *et al.* 2017). Finally, we investigate the dependence of the far-field sound pressure level (SPL) and directivity pattern on the Mach number.

The paper is organized as follows. The acoustic source term and its decomposition are described in § 2. Section 3 is dedicated to the numerical set-up. Section 4 addresses the results and discussion, and finally conclusions are drawn in § 5.

2. Theoretical framework

The conservative form of the governing equations for compressible, Newtonian fluid flow in an inertial frame of reference without external forces can be written as

$$\frac{\partial \rho}{\partial t} + \frac{\partial}{\partial x_j}(\rho v_j) = 0, \tag{2.1}$$

$$\frac{\partial \rho v_i}{\partial t} + \frac{\partial}{\partial x_j}(\rho v_i v_j) = \frac{\partial \sigma_{ij}}{\partial x_j}, \tag{2.2}$$

$$\frac{\partial \rho e_T}{\partial t} + \frac{\partial}{\partial x_j}(\rho e_T v_j) = \frac{\partial v_i \sigma_{ij}}{\partial x_j} - \frac{\partial q_j}{\partial x_j}, \tag{2.3}$$

where ρ is density, t is time and v_j is the velocity component in the x_j direction. Here σ_{ij} is the stress tensor and is given as

$$\sigma_{ij} = -P\delta_{ij} + \tau_{ij} = -P\delta_{ij} + 2\mu S_{ij} + \lambda S_{mm}\delta_{ij}, \tag{2.4}$$

where P is the static pressure, δ_{ij} is the Kronecker delta tensor, $\tau_{ij} = 2\mu S_{ij} + \lambda S_{mm}\delta_{ij}$ is the fluid-dynamic contribution to the stress tensor and is called the deviatoric stress tensor, μ is the shear viscosity coefficient, $S_{ij} = \frac{1}{2}(\partial v_i/\partial x_j + \partial v_j/\partial x_i)$ is the strain rate tensor, $\lambda = \mu_v - 2\mu/3$ is the second viscosity coefficient and μ_v is the bulk viscosity coefficient which is often assumed to be zero, $\mu_v = 0$, based on the Stokes assumption.

In the conservation of energy equation (2.3), $e_T = e + \frac{1}{2}v_i v_i$ is the total energy per unit mass, e is the internal energy per unit mass and q_j is the heat flux component in the x_j direction. We neglect radiation and assume that the heat transfer follows Fourier's law of heat conduction, $q = -k\nabla T$, where q is the heat flux, k is the thermal conductivity of the fluid and T is temperature. Considering a calorically perfect gas relation, $e = C_v T$ and $P = \rho R T$, where C_v is the specific heat capacity at constant volume and R is the gas constant, the above conservation equations can be solved.

By combining the continuity and momentum equations, Lighthill's inhomogeneous wave equation is derived (Lighthill 1952). The homogeneous part of this partial differential equation describes acoustic wave propagation within an inviscid, stationary fluid whereas the inhomogeneous contribution represents the summation of all source terms driving the wave. The equation can be written as follows:

$$\frac{\partial^2 \rho}{\partial t^2} - c_0^2 \nabla^2 \rho = \nabla \cdot \underbrace{\left[\rho(v \cdot \nabla)v - v\frac{\partial \rho}{\partial t} + (\nabla P - c_0^2 \nabla \rho) - \nabla \cdot \tau \right]}_{S}, \tag{2.5}$$

where the left-hand side is the wave operator with c_0 as the constant speed of sound of the stationary medium and ρ, density, as the dependent variable. The right-hand side is the source term (S) where v is the velocity vector. The acoustic source term can be

reformulated to delineate the physical interpretation of the mechanisms causing the sound generation as

$$\frac{\partial^2 \rho}{\partial t^2} - c_0^2 \nabla^2 \rho = \underbrace{\boldsymbol{\nabla} \cdot [\rho(\boldsymbol{\omega} \times \boldsymbol{v})]}_{A} + \underbrace{\boldsymbol{\nabla} \cdot \left[\rho \frac{\boldsymbol{\nabla}|\boldsymbol{v}|^2}{2}\right]}_{B} + \underbrace{\boldsymbol{\nabla} \cdot [(\boldsymbol{\nabla} \cdot (\rho \boldsymbol{v}))\boldsymbol{v}]}_{C}$$

$$+ \underbrace{(\nabla^2 P - c_0^2 \nabla^2 \rho)}_{D} \underbrace{-\boldsymbol{\nabla} \cdot [\boldsymbol{\nabla} \cdot \tau]}_{E}, \tag{2.6}$$

where $\boldsymbol{\omega} = \boldsymbol{\nabla} \times \boldsymbol{v}$ is the vorticity vector. This reformulation of the Navier–Stokes equations, (2.6), is exact and, unlike standard aeroacoustic analogies, all acoustic source terms are preserved. The wave operator can also be written in terms of pressure as the dependent variable; however, since it is computationally inefficient, we proceed with the above form of Lighthill's equation. The decomposed terms in (2.6) are tractable and amenable to a physical interpretation. Term A denotes the role of the divergence of the Lamb vector, $\boldsymbol{\omega} \times \boldsymbol{v}$, term B is related to the spatial variation of the kinetic energy, term C contains interactions involving the gradient of density and the dilatation field, term D is the deviation from the isentropic condition and term E contains the viscous effects. Through a further expansion of each of these terms, the individual contribution of the velocity, vorticity, dilatation and density and their mutual interactions can be delineated even more:

$$\underbrace{\boldsymbol{\nabla} \cdot [\rho(\boldsymbol{\omega} \times \boldsymbol{v})]}_{A} = \underbrace{(\rho\boldsymbol{v}) \cdot (\boldsymbol{\nabla} \times \boldsymbol{\omega})}_{A1} + \underbrace{\boldsymbol{v} \cdot (\boldsymbol{\nabla}\rho \times \boldsymbol{\omega})}_{A2} \underbrace{-\rho(\boldsymbol{\omega} \cdot \boldsymbol{\omega})}_{A3}, \tag{2.7}$$

$$\underbrace{\boldsymbol{\nabla} \cdot \left[\rho \frac{\boldsymbol{\nabla}|\boldsymbol{v}|^2}{2}\right]}_{B} = \underbrace{\rho \nabla^2 \left(\frac{|\boldsymbol{v}|^2}{2}\right)}_{B1} + \underbrace{\boldsymbol{\nabla}\rho \cdot \boldsymbol{\nabla} \frac{|\boldsymbol{v}|^2}{2}}_{B2}, \tag{2.8}$$

$$\underbrace{\boldsymbol{\nabla} \cdot [(\boldsymbol{\nabla} \cdot (\rho\boldsymbol{v}))\boldsymbol{v}]}_{C} = \underbrace{\rho\boldsymbol{v} \cdot \boldsymbol{\nabla}(\boldsymbol{\nabla} \cdot \boldsymbol{v})}_{C1} + \underbrace{\rho(\boldsymbol{\nabla} \cdot \boldsymbol{v})^2}_{C2} + \underbrace{2(\boldsymbol{\nabla} \cdot \boldsymbol{v})\boldsymbol{v} \cdot \boldsymbol{\nabla}\rho}_{C3}$$

$$+ \underbrace{\boldsymbol{v} \cdot (\boldsymbol{v} \cdot \boldsymbol{\nabla}\boldsymbol{\nabla}\rho)}_{C4} + \underbrace{\boldsymbol{v} \cdot (\boldsymbol{\nabla}\rho.\boldsymbol{\nabla}\boldsymbol{v})}_{C5}, \tag{2.9}$$

$$\underbrace{(\nabla^2 P - c_0^2 \nabla^2 \rho)}_{D} = \underbrace{\nabla^2 P}_{D1} \underbrace{-c_0^2 \nabla^2 \rho}_{D2}, \tag{2.10}$$

$$\underbrace{-\boldsymbol{\nabla} \cdot [\boldsymbol{\nabla} \cdot \tau]}_{E} = \underbrace{-\frac{4}{3}\mu\nabla^2(\boldsymbol{\nabla} \cdot \boldsymbol{v})}_{E1} \underbrace{-\boldsymbol{\nabla}\mu \cdot \left[\frac{4}{3}\boldsymbol{\nabla}(\boldsymbol{\nabla} \cdot \boldsymbol{v}) - \boldsymbol{\nabla} \times \boldsymbol{\omega}\right] - \boldsymbol{\nabla} \cdot \boldsymbol{\xi}}_{E2}, \tag{2.11}$$

where μ is the dynamic viscosity, $\boldsymbol{\xi} = 2\boldsymbol{S} \odot \boldsymbol{\nabla}\mu - 2/3(\boldsymbol{\nabla} \cdot \boldsymbol{v})\boldsymbol{\nabla}\mu$ with $\boldsymbol{S}$ as the strain rate tensor and term E2 shows the effect of the viscosity variation.

Let us consider the terms in the above reformulation. If the flow is assumed to be inviscid, incompressible and isentropic, only terms A1, A3 and B1 remain. Term A1 is the flexion product and is primarily positive since it represents a dissipative mechanism with a minus sign in the kinetic energy transport equation of incompressible flow (Hamman,
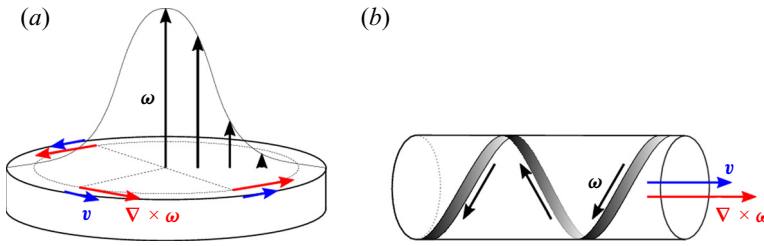
Figure 2. Qualitative orientation of the velocity and flexion vectors (*a*) at the edge of a vortex tube with Gaussian vorticity distribution and (*b*) in the core of a twisted vortex tube, resulting in an unwinding of the vortex line.

Klewicki & Kirby 2008):

$$\frac{1}{2}\frac{\partial |\boldsymbol{v}|^2}{\partial t} = -\boldsymbol{v}\cdot\nabla\phi - \nu\boldsymbol{v}\cdot(\nabla\times\boldsymbol{\omega}),\tag{2.12}$$

where $\phi = P/\rho + |\boldsymbol{v}|^2/2$ and ν are the Bernoulli function and kinematic viscosity, respectively. The flexion product has been also considered as an unwinding term, converting the angular momentum in a vortex into linear momentum, thus attenuating the low pressure in the vortex core (Hamman *et al.* 2008). Further, it can be related to the Laplacian of the solenoidal velocity vector by $\boldsymbol{v}\cdot(\nabla\times\boldsymbol{\omega}) = -\boldsymbol{v}\cdot\nabla^2\boldsymbol{v}$; see figure 2 for a qualitative orientation of the velocity and flexion (curl of vorticity) vectors at the edge of a vortex tube with Gaussian vorticity distribution and in the core of a twisted vortex tube. Term A3 is enstrophy and its contribution to the source term is always negative. Term B1 is the Laplacian of the kinetic energy highlighting the role of the kinetic energy deviation from its local average in the sound production. Given the satisfactory results of the low-Mach-number approximation in sound predictions (Golanski, Fortuné & Lamballais 2005), it is natural to conjecture that terms A1, A3 and B1 are the dominant hydrodynamic sources of sound. In this regard, Cabana, Fortuné & Jordan (2008) solved a one-dimensional wave equation for each of the decomposed source terms (except the viscous terms) and showed that terms A2 and B2 are also important in sound production in a mixing layer. They categorized terms A and B as production terms, and term C – involving interactions of density, velocity and dilatation fields – as the acoustic term responsible for the sound propagation. Furthermore, vortex sound analogies consider only terms A and B providing suitable sound predictions (Powell 1964) – in high-*Re*, low-Mach-number flows, term B is often neglected. Although the aeroacoustic analogies (e.g. Möhring's or Lighthill's) hinge on an *ad hoc* simplification of the acoustic source term and the decoupling of the sound production and propagation mechanisms, elimination of any physical subtleties in the acoustic–hydrodynamic interactions could affect accurate assessment of the propagated sound (Coiffet *et al.* 2006). In this study, we analyse the evolution of the entire source term and its dominant components during vortex reconnection.

3. Numerical set-up

Although reconnection has been studied for different configurations, e.g. vortex rings (Kida, Takaoka & Hussain 1991) and orthogonal vortices (Boratav, Pelz & Zabusky 1992), many studies focus on anti-parallel vortices with a localized perturbation (Melander & Hussain 1988). It has been shown that mutual induction between two approaching
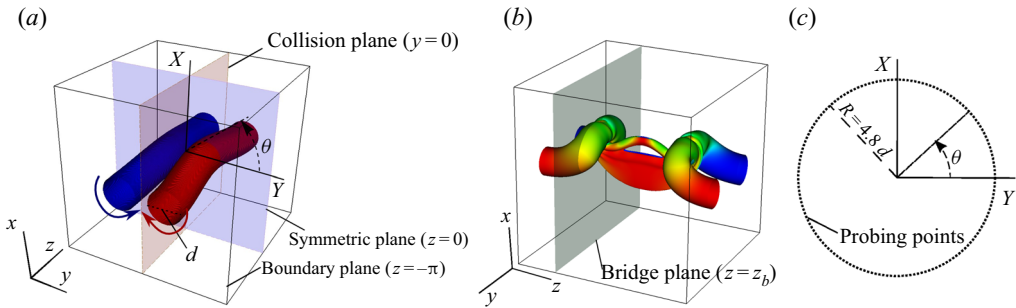
Figure 3. (*a*) Initial configuration. (*b*) Bridge plane. (*c*) Probing points on symmetric and boundary planes. Modified version of figure 1 of Daryan *et al.* (2020).

vortex filaments leads to local anti-parallel orientation (Siggia 1985; Kida & Takaoka 1987, 1994), and as a result, the anti-parallel configuration could be considered as the representative canonical flow of reconnection revealing the underlying physics of this phenomenon. Also, this simple set-up, which can be thought of as an abstraction of a Crow instability (Crow 1970), isolates the reconnection enabling high-resolution simulations and emergence of the fundamental features.

Using the same numerical set-up as Daryan *et al.* (2020), initial anti-parallel vortex tubes with a sinusoidal perturbation are simulated in a large computational domain. Initial vorticity field follows the compact Gaussian vorticity distribution (Virk *et al.* 1995; Melander & Hussain 1988) given by

$$
\left.
\begin{aligned}
\boldsymbol{\omega}(\boldsymbol{x}) &= \omega(r)(-A\sin(\alpha)\sin(z)\boldsymbol{i} + A\cos(\alpha)\sin(z)\boldsymbol{j} + \boldsymbol{k}), \\
\omega(r) &= \begin{cases} 10[1 - f(r/r_c)], & r < r_c, \\ 0, & r \geqslant r_c, \end{cases} \\
r^2 &= (x - x_c - A\sin(\alpha)\cos(z))^2 + (y - y_c + A\cos(\alpha)\cos(z))^2, \\
f(\eta) &= \exp[-K\eta^{-1}\exp(1/(\eta - 1))], \quad K = \tfrac{1}{2}\exp(2)\log(2),
\end{aligned}
\right\}
\tag{3.1}
$$

where A is the sinusoidal perturbation amplitude, α is the inclination angle (the angle of each vortex axis, projected on the x–y plane, with the negative direction of the y axis), r_c is the radius and $(x_c + A\sin(\alpha)\cos(z), y_c - A\cos(\alpha)\cos(z), z)$ is the centre of the vortex tube ((x_c, y_c) is the centre of each vortex tube on the $z = \pi/2$ plane). In the current study these parameters are set as: $A = 0.2$, $\alpha_1 = \pi/3$, $\alpha_2 = 2\pi/3$, $r_c = 0.65$, $x_{c1} = x_{c2} = 0$, $y_{c1} = 0.75$ and $y_{c2} = -0.75$, leading to two anti-parallel perturbed vortices at the middle of a large computational domain; see figure 3(*a*). The perturbation without a gap between the compact vortex cores in the kink section localizes the reconnection event. Figure 3(*a*) also shows characteristic planes, i.e. symmetric plane ($z = 0$), boundary plane ($z = -\pi$) and collision plane ($y = 0$). Also, the bridge plane is defined at $z = z_b$, where z_b locates the maximum ω_y on the collision plane and $-\pi < z_b < 0$; see figure 3(*b*).

To analyse the far-field sound, two sets of 192 equidistant probing points with circular layout are considered on symmetric and boundary planes; the centres of the circles are respectively at $(x_s, 0, 0)$ and $(x_s, 0, -\pi)$, where $x_s = 1.38$ is the x with the maximum absolute value of the source term at the beginning of the circulation transfer at the reference Mach number of $M_o = 0.5$ – the location is the same for all M_o

under consideration. The probing points are located on a circle of radius $R = 4.8d$, where $d = 2r_c$ is the diameter of the initial vortex tubes; see figure 3(*c*).

We implement periodic boundary conditions in all three directions. To avoid polluting the data collected at the probing points by information across the periodic boundaries, the computational domain is well extended in the advection (*x*) and lateral (*y*) directions. Considering the higher relative speed of sound at lower Mach number, the domain size is set to $66\pi \times 66\pi \times 2\pi$ for $M_o = 0.1$ and $28\pi \times 28\pi \times 2\pi$ for all other M_o. The mesh size of the inner $(2\pi)^3$ domain is 384^3, which is consistent with our mesh independence at $Re = 1500$ (Daryan *et al.* 2020). By applying expansion growth ratio = 1.01 for the surrounding domain, the final resolution becomes $1212 \times 1212 \times 384$ for $M_o = 0.1$ and $1036 \times 1036 \times 384$ for all other M_o.

To minimize the initial acoustic transients and capture the salient features at early stages of compressible reconnection, we use the polytropic initial condition proposed by Virk & Hussain (1993). Using the initial vorticity distribution (3.1), the velocity field is determined by solving the Poisson equation: $\nabla^2 \boldsymbol{v} = -\nabla \times \boldsymbol{\omega}$. The velocity field is then normalized by the maximum velocity (the point with the maximum velocity is considered as the reference point and is denoted by the subscript *o*). Imposing incompressible and inviscid flow assumptions, the Poisson equation for the pressure term can be derived by taking the divergence of the momentum equation, i.e. $\nabla \cdot (\nabla P/\rho) = -\nabla \cdot [(\boldsymbol{v} \cdot \nabla)\boldsymbol{v}]$. Density is substituted by a polytropic relation, i.e. $\rho = (P/P_o)^{1/\gamma}$, where $P_o = 1/\gamma M_o^2$ is the pressure at the reference point, $\gamma = 1.4$ is the ratio of the specific heats and M_o is the Mach number at the reference point. The Poisson equation provides the pressure difference; the pressure field is updated such that pressure at the reference point becomes P_o. Finally, density is calculated by the polytropic relation satisfying $\rho_o = 1$. Thermodynamic variables follow the ideal gas equation, $P = \rho R T$, where $R = P_o$ is the gas constant, implying $T_o = 1$. The initial velocity field is the same for all cases studied in this paper; to get different reference Mach numbers, M_o, we change P_o leading to the modification of the speed of sound at the reference point, i.e. $c_o = V_o/M_o = \sqrt{\gamma P_o/\rho_o}$, where $V_o = 1$ is the velocity at the reference point. In the current study, we consider five different subsonic reference Mach numbers: $M_o = 0.1, 0.3, 0.5, 0.7$ and 0.9.

The vortex Reynolds number is defined as $Re = \Gamma_0/\nu_o$, with Γ_0 the initial circulation of either vortex and ν_o the kinematic viscosity at the reference point. The dynamic viscosity obeys the power-law relation $\mu = \mu_o(T/T_o)^{3/4}$, where $\mu_o = \rho_o \nu_o$. In the current study, the Reynolds number is fixed at $Re = 1500$.

The reference length and time are taken to be unity. Time t_0 represents the time just before the beginning of the circulation transfer. Start time, t_S, and end time, t_E, are defined as the times when the circulation on half of the symmetric plane ($z = 0, y > 0$) becomes $\Gamma = 0.95\Gamma_0$ and $\Gamma = 0.05\Gamma_0$, respectively. The reconnection time, t_R, is the time required for the reduction of the circulation on half of the symmetric plane from $\Gamma = 0.95\Gamma_0$ to $\Gamma = 0.50\Gamma_0$. Furthermore, the maximum time, t_M, is defined as the moment when the absolute value of the acoustic source term becomes maximal (after the start of reconnection $t_M > t_S$) within the computational domain.

Direct simulation of the compressible Navier–Stokes equations is performed using the Hybrid solver (Bermejo-Moreno *et al.* 2013). The solver uses a fourth-order Runge–Kutta scheme for time integration and a sixth-order finite-difference scheme for spatial derivatives combined with a high-order filtering following Ducros *et al.* (2000). The code has been used and validated for shock–turbulence interaction (Larsson, Bermejo-Moreno & Lele 2013), turbulent channel flows (Trettel & Larsson 2016) and other canonical flows.

933 A34-8

M_o	Characteristic moments							Characteristic intervals		
	t_0	t_S	$t_S + 1.5t_R$	t_E	t_M	$t_E + 2t_R$	$t_E + 4t_R$	t_R	$t_E - t_S$	$t_M - t_E$
0.1	6.34	7.16	9.14	9.62	9.91	12.62	15.62	1.50	2.46	0.29
0.3	6.41	7.26	9.24	9.71	10.01	12.69	15.67	1.49	2.45	0.30
0.5	6.56	7.44	9.42	9.88	10.25	12.88	15.88	1.50	2.44	0.37
0.7	6.75	7.70	9.69	10.13	10.90	13.15	16.17	1.51	2.43	0.77
0.9	4.29	7.83	10.16	10.58	11.57	14.26	17.94	1.84	2.75	0.99

Table 1. Characteristic times for different M_o.

4. Results and discussion

Table 1 shows the characteristic times for the different M_o. An increase of M_o postpones reconnection in these initially subsonic cases. More precisely, t_S and t_E increase as M_o increases. Yet, with the exception of the $M_o = 0.9$ case, the time required for the circulation transfer during subsonic reconnection (t_R and $t_E - t_S$) is independent of M_o; however, $t_M - t_E$ increases with M_o.

The reduction of t_0 at $M_o = 0.9$ is due to the formation of shocklets which lead to an earlier circulation transfer; Virk *et al.* (1995) observed the initial circulation transfer due to shock formation in the supersonic regime. However, these shocklets (at the current *Re*) are not strong enough to modify the reconnection process. The shocklet formation stems from the jet flow on the collision plane which is intensified as the two vortices approach each other by self-induction. Intensification of the maximum local Mach number, M_{max}, during reconnection can be seen in figure 4(*a*). For $M_o = 0.9$, prior to the start of reconnection, M_{max} crosses the sonic threshold and rises up to $M_{max} \approx 1.6$; the extremum of other cases takes place just after t_S. Once reconnection begins, the reversed flow induced by the reconnected vortex lines, which are accumulated at the bridges, slows down the jet flow and impedes further growth of the local Mach number (while also slowing down the tenting phenomenon of the vortex pair, hence slowing their collision and also the circulation transfer rate). By only considering the states after the start of reconnection, figure 4(*b*) shows a linear scaling of the overall maximum local Mach number, $M_{overall\,max} \approx 1.5M_o$, at $Re = 1500$; 'overall max' refers to the maximum over the time period of $[t_S, t_E + 4t_R]$. Mach number M_{max} does not necessarily always occur at the same location. Figure 5 shows the evolution of the regions with a high local Mach number for the $M_o = 0.5$ case. Initially located at the contact point between the vortices, they gradually migrate towards the bridges; owing to the initial jet flow followed by the sharp cusp-induced rapid repulsion of the bridges, high velocity is expected at theses areas. Note that due to the qualitative similarities in all the initially subsonic reconnection cases at $Re = 1500$, we observe the same general local Mach number distribution at other cases after t_S (discussed later).

We expect that shocklets become stronger at higher *Re* as the jet flow between the two vortices intensifies before the start of reconnection – this complex issue is a focus of a separate investigation. We speculate that these shocklets may be a defining feature of the reconnection mechanism at high *Re*, which not only alter the reconnection dynamics, but can also play a significant role in sound generation; near shocklets, we expect magnification of the gradient of density, the dilatation and their interactions which appeared in source term C in (2.9). Clearly, despite a subsonic M_o, reconnection would affect shock formation which in turn modifies the circulation transfer process
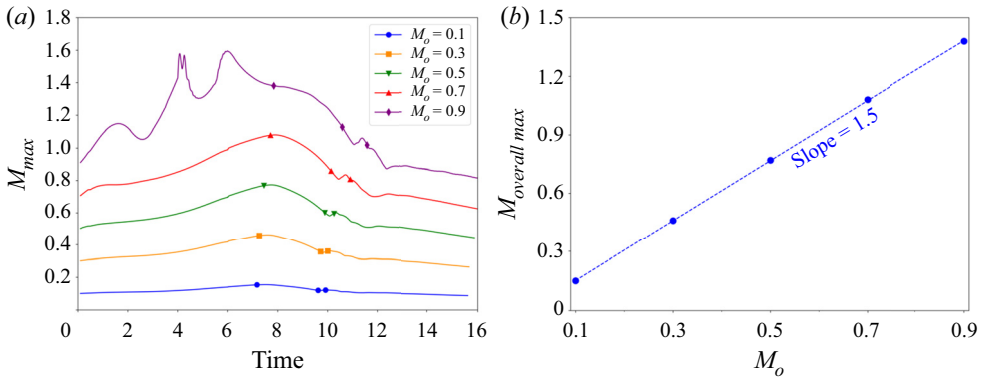
Figure 4. (*a*) Evolution of M_{max}. Markers represent t_S, t_E and t_M. (*b*) Scaling of $M_{overall\,max}$.
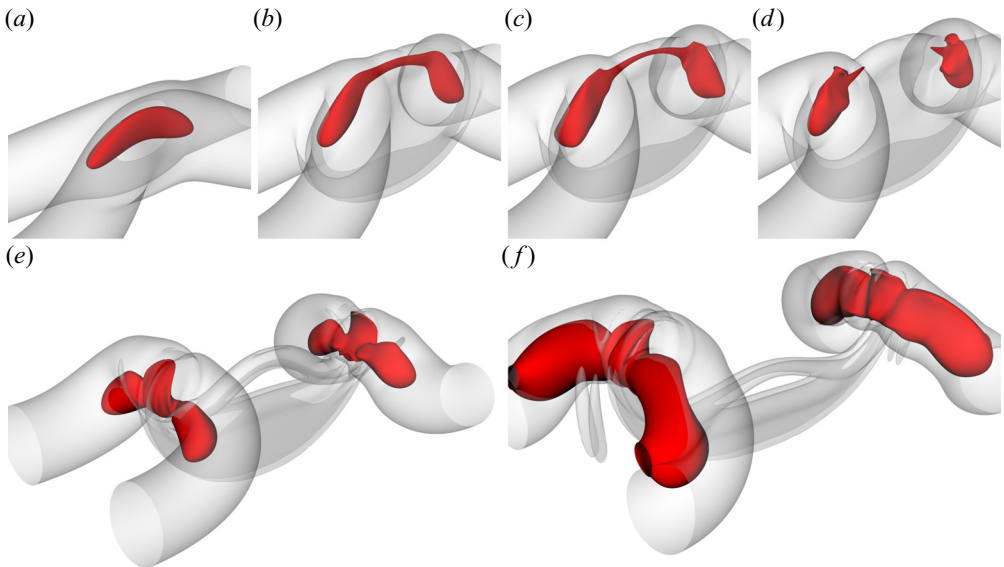

Figure 5. Local Mach number isosurface (red colour) of $M_o = 0.5$ set at 80 % of its maximum value at (*a*) t_S, (*b*) $t_S + 1.5t_R$, (*c*) t_E, (*d*) t_M, (*e*) $t_E + 2t_R$ and (*f*) $t_E + 4t_R$. Grey transparent colour shows the enstrophy isosurface set at 2 % of the overall maximum enstrophy. A magnified view is presented in (*e*,*f*).

(Virk *et al.* 1995). In the following sections, we limit our discussion to the period after the start of the reconnection, i.e. after t_S.

4.1. *Source term evolution*

The order of magnitude of the convective term in the wave operator of Lighthill's equation (left-hand side of (2.5)) depends on the square of the reference speed of sound. As a result, in all scale analyses, we consider the relative source term, divided by c_o^2. The evolution of the extrema (minimum and maximum at each time) of the source term in (2.5) at different M_o is presented in figure 6(*a*). Apart from the initial oscillations at $M_o = 0.9$ which are tied to the formation of shocklets, the most obvious commonality among all

933 A34-10
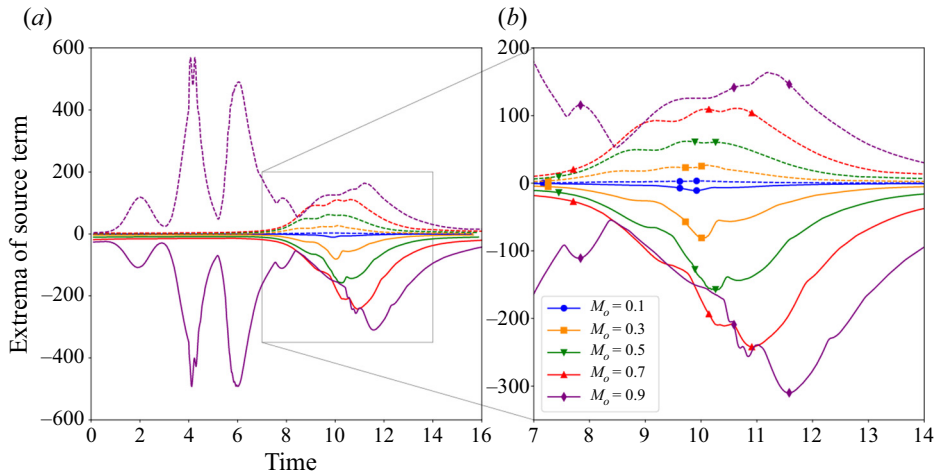
Figure 6. (*a*) Evolution of the minimum (solid line) and maximum (dashed line) of the source term. Markers represent t_S, t_E and t_M. (*b*) Magnified view.
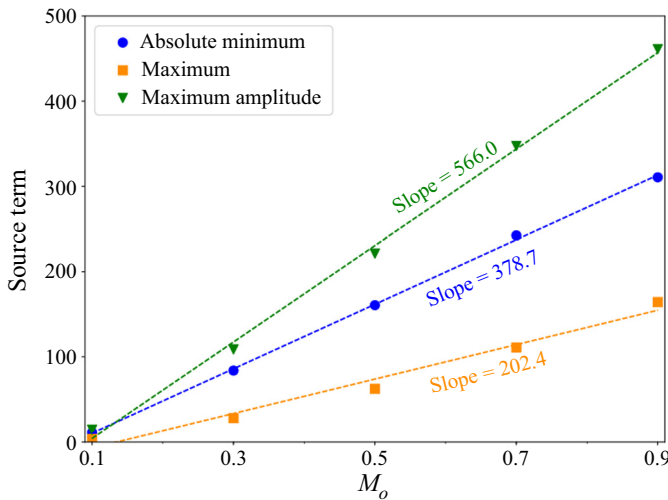
Figure 7. Scaling of the overall extrema and maximum amplitude of the source term.

cases is the amplification of the source strength during reconnection; see the magnified plot of figure 6(*b*).

Just after t_E, once circulation transfer is complete, the accumulation of the cusped reconnected vortex lines reinforces the self-induced rapid repulsion of the fully developed bridges, culminating in the maximum absolute value of the source term at t_M. Linear growth of the overall extrema and maximum amplitude (largest difference between the local minimum and maximum) of the source term with respect to M_o is evident in figure 7.

To identify the dominant components of the source term, we examine the respective contribution of each term on the right-hand side of (2.6) through an order-of-magnitude analysis. The extrema evolution of these terms at $M_o = 0.1$ and $M_o = 0.9$ is provided in figure 8; similar to the source term (S), the amplifications of the individual components during reconnection are quite different. Term A, the divergence of the Lamb vector,
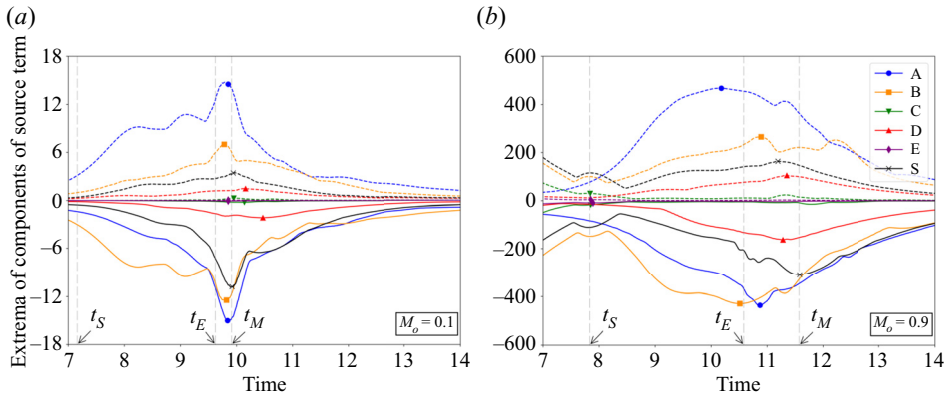
Figure 8. Evolution of the minimum (solid line) and maximum (dashed line) of the components of the source term at (*a*) $M_o = 0.1$ and (*b*) $M_o = 0.9$. Markers represent the overall extrema.

and term B, chiefly related to the Laplacian of the kinetic energy, are the dominant hydrodynamic components – these terms are also considered as the main sound production mechanisms in the vortex sound analogy (Powell 1964). Term D, the deviation from the isentropic condition, also has a notable contribution; this term is generally neglected in aeroacoustic analogies (Powell 1964). Terms C and E, respectively containing dilatation and viscous effects, become negligible after the start of reconnection (t_S). Nonetheless, by virtue of the sharp velocity changes through the shocklets, we expect term C to play an inevitable role prior to the start of reconnection for the $M_o = 0.9$ case. The detailed study of the shocklet formation during viscous vortex reconnection and its impact on the far-field noise will be left to future work.

Figure 8 shows that compressibility leads to smoother changes of the extrema of the source term and its components during the time interval [t_E, t_M]. In figure 8(*a*), at $M_o = 0.1$, sharp repulsion and large temporal variations of the extrema of the source terms are clear near t_E. On the other hand, smoother variations can be seen in figure 8(*b*) at $M_o = 0.9$. Also, the overall extrema of terms A and B at $M_o = 0.1$ take place in the time interval of $t_E < t < t_M$, which is not always true for $M_o = 0.9$.

Using (2.7) and (2.8), we can further decompose terms A and B. Figure 9 shows the evolution of the extrema of the decomposed components of the source term, while terms C and E are excluded for clarity. Terms A2 and B2 do not play a considerable role. The flexion product, term A1, enstrophy, term A3, and the Laplacian of the kinetic energy, term B1, are dominant. The maximum of flexion product is always more than its absolute minimum value. Also, whereas the overall extrema of the dominant terms generally occur close to the end of reconnection, flexion product takes its overall minimum with a delay after t_M, when the bridges are recoiling from each other. As also revealed in figure 8, sharp and smooth variations near t_E can be observed in figures 9(*a*) and 9(*b*) at low and high M_o, respectively.

Let us examine each of these dominant decomposed components individually. The evolution of the bounds of terms A1, A3, B1 and D with respect to M_o is presented in figure 10. Compressibility intensifies all of these terms. Except for the overall minimum of term A1 which occurs after t_M, the overall extrema take place close to t_E, generally for $t_E < t < t_M$ – note that at $M_o = 0.7, 0.9$, the overall minimum of term B1 occurs just before t_E. The effect of M_o is more obvious on the evolution of term D extrema – the overall extrema occur before and after t_M at high and low M_o, respectively. As depicted in
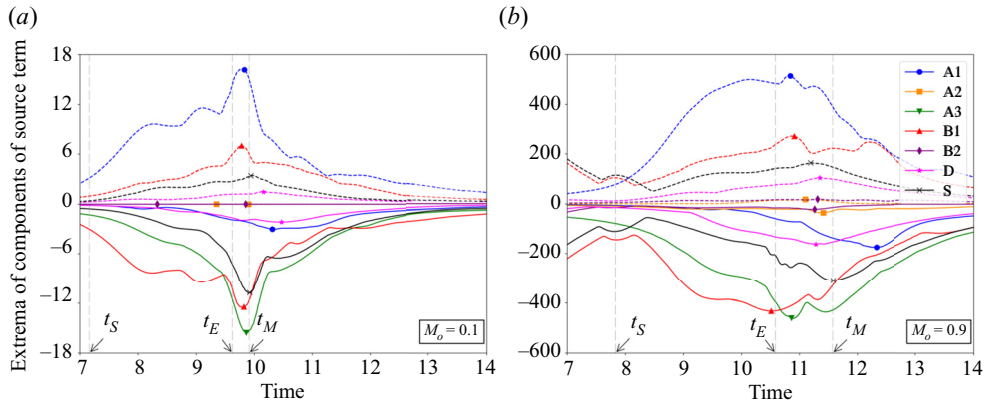
Figure 9. Evolution of the minimum (solid line) and maximum (dashed line) of the decomposed components of the source term at (*a*) $M_o = 0.1$ and (*b*) $M_o = 0.9$. Markers represent the overall extrema.
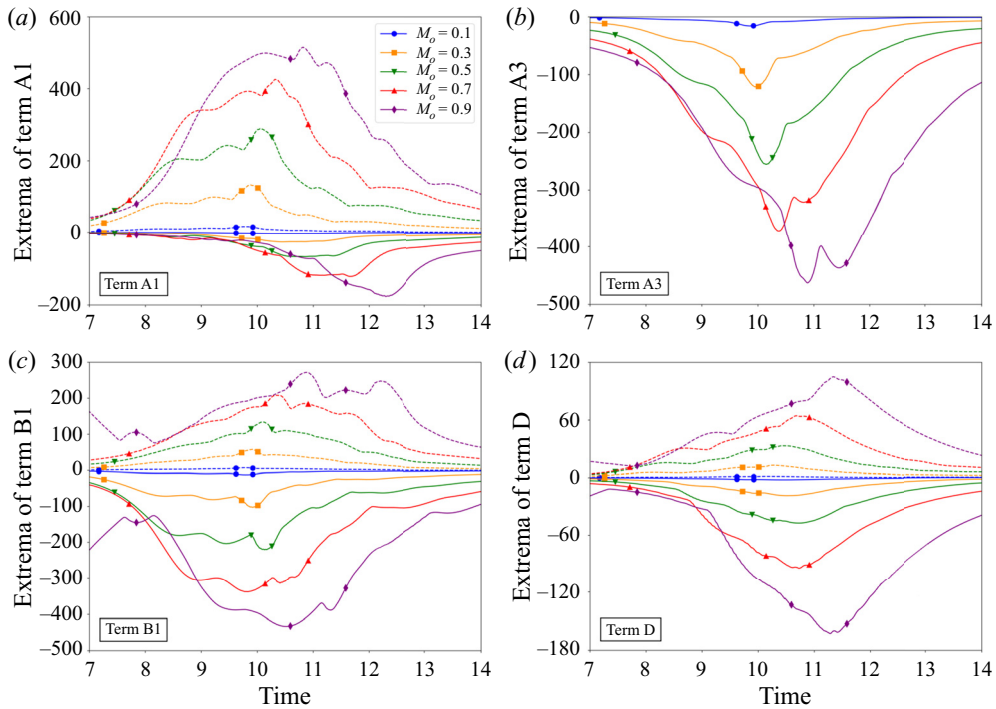

Figure 10. Evolution of the minimum (solid line) and maximum (dashed line) of (*a*) term A1, (*b*) term A3, (*c*) term B1 and (*d*) term D. Markers represent t_S, t_E and t_M.

figure 10, the contribution of the flexion product to the source term is mainly positive. Of course, the enstrophy term is always negative. The Laplacian of the kinetic energy and the deviation from the isentropic condition have both positive and negative effects (discussed later).

Similar to the source term (figure 7), the overall extrema and maximum amplitude of the dominant terms are linearly scaled by M_o as depicted in figure 11(*a*–*c*). Although many of these terms contain a second-order dependence on the velocity perturbation, the scaling
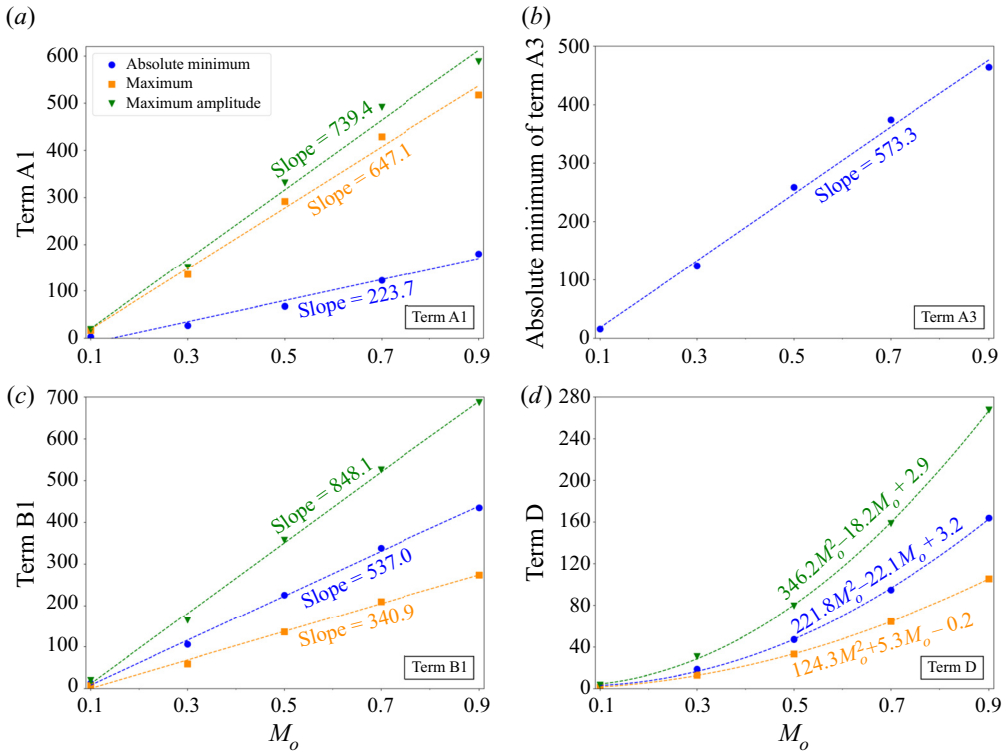
Figure 11. Scaling of the overall extrema and maximum amplitude of (*a*) term A1, (*b*) term A3, (*c*) term B1 and (*d*) term D.

of the overall maximum of these terms is linear, suggesting that the higher compressibility dampens the maximum velocity during reconnection. This is further supported by the scaling of term D. Term D, which contains the Laplacian of pressure and density, follows a quadratic scaling relation; see figure 11(*d*). Such second-order dependency of term D on compressibility implies significant deviation from the isentropic condition at higher M_o. As vortex reconnection gives rise to important thermodynamic changes it is expected that we observe a departure from the isentropic condition, especially at higher M_o. It should be noted that the effect of entropic inhomogeneities on sound generation may actually be larger in other right-hand-side terms (see e.g. Yang, Guzmán-Iñigo & Morgans 2020).

Correspondingly, the aeroacoustic analogies, which generally neglect this term at low Mach number, appear to incorrectly estimate the acoustic source term (discussed later). Relatively little is known about the role of the deviation from the isentropic condition in sound production. At the end of our order-of-magnitude analysis, by comparing the magnitude of the overall extrema and maximum amplitude shown in figures 10 and 11, we can conclude that the Laplacian of the kinetic energy, flexion product, enstrophy and deviation from the isentropic condition are, successively in decreasing magnitude, the dominant components of the source term during reconnection. Note that such an analysis only highlights the pointwise significance of these terms; of course, a high value of a term at a single point in the domain does not necessarily imply the integrated importance of that term.

As mentioned above, the flexion product, represented by term A1, is one of the dominant sources of aeroacoustic noise associated with the hydrodynamics of reconnection.
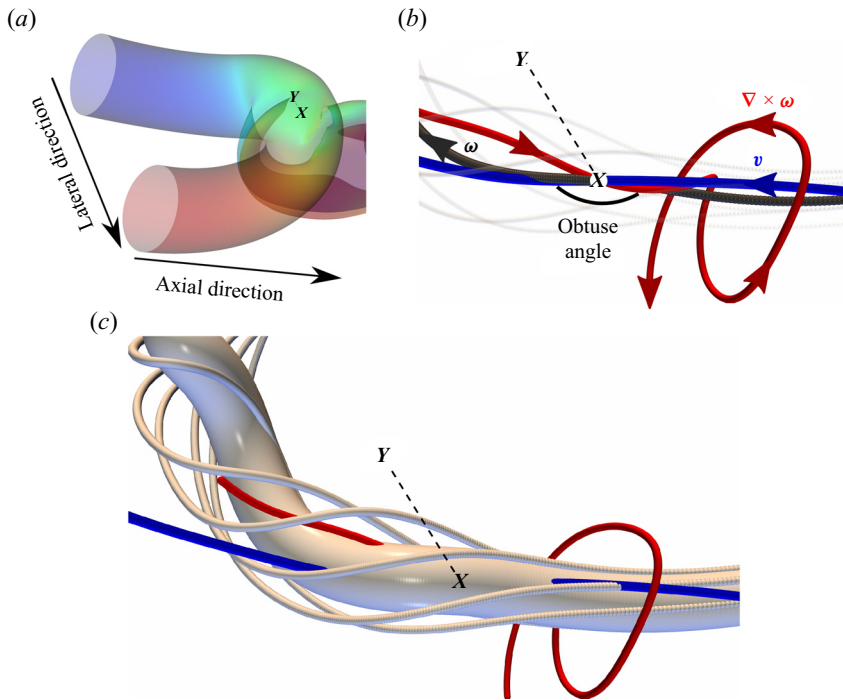
Figure 12. (*a*) Position of the overall minimum flexion product at $M_o = 0.5$. (*b*) Orientation of the velocity, vorticity and flexion vectors. (*c*) Twist of vortex lines (small light-coloured lines) around the central vortex tube.

Figure 2(*a*) shows that in a prototypical vortex tube, the flexion ($\nabla \times \boldsymbol{\omega}$) and local velocity are co-aligned in the azimuthal direction. As a result, at a given radial distance from the axis of a vortex tube, the flexion product $\boldsymbol{v} \cdot (\nabla \times \boldsymbol{\omega})$ is constant and always has a positive value. Alternatively, if the vortex tube is twisted (as in a polarized vortex, i.e. a vortex with axial flow), as shown in figure 2(*b*), and has a self-induced core or advective velocity along the tube, the flexion and local velocity vectors will be aligned with the twisted vortex tube, thus yielding a large flexion product. These two scenarios, shown in figure 2(*a*,*b*), are means of flexion product generation in prototypical vortices. Following Hamman *et al.* (2008), we also speculate that the largest flexion product will result in coiling (negative flexion product) or uncoiling (positive flexion product) of the twisted vortex tube. Results in figure 10(*a*) show that the overall maximum and minimum of the flexion product occur after t_E and physically correspond to an axial advection of a twisted vortex tube. The uncoiling motion is intensified near t_E by the repulsion of the highly curved vortex lines at the top of the bridges. The maximum coiling (or the flexion product overall minimum) occurs at the region where twisted filaments wrap around the bridges. The coiling mechanism is visualized at $M_o = 0.5$ in figure 12; the location of the overall minimum flexion product is shown in figure 12(*a*) and the orientations of the velocity, vorticity and flexion vectors about this point are shown in figure 12(*b*,*c*). In figure 12(*b*), the velocity and flexion vectors form a very large obtuse angle, thus yielding the maximum negative value of the flexion product. The orientation of the flexion vector at this location is the result of the twisting of the vortex lines bundle about the vortex tube axis, whereas the velocity vector (which is dominated by the repulsion of the bridges) is nearly aligned with the flexion vector, albeit in the opposite direction. Interestingly, as illustrated in figure 2(*a*)
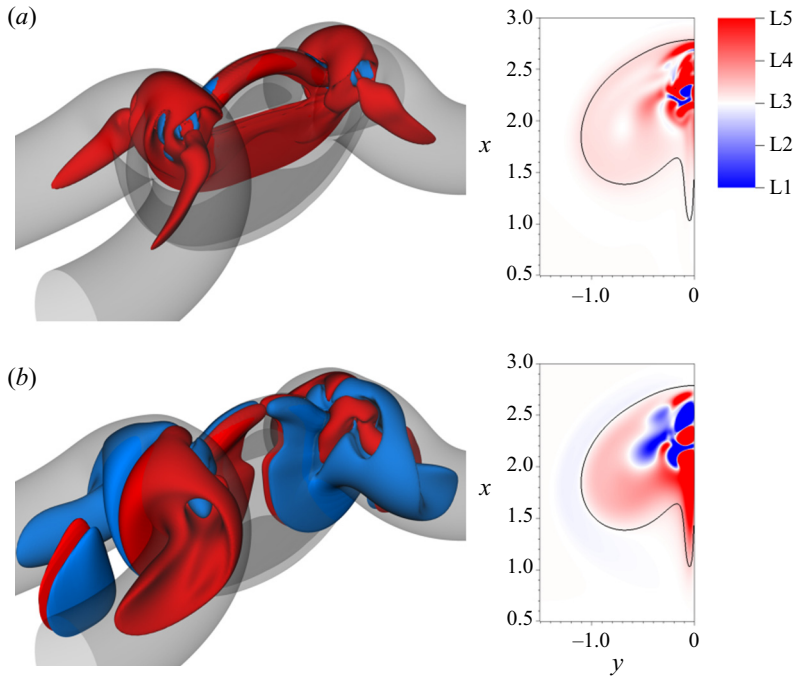
Figure 13. Positive and negative isosurface and contour (on the half of the bridge plane) of (*a*) flexion product and (*b*) helicity density for $M_o = 0.5$ at the time of the overall minimum of the flexion product. Blue and red isosurface levels equal the negative and positive 1 % of the overall maximum absolute value of each variable. Grey transparent colour shows the enstrophy isosurface set at 2 % of the overall maximum enstrophy. Limits of the global linear legend equal the negative and positive 5 % of the overall maximum absolute value of each variable. The solid line depicts the enstrophy contour set at 2 % of the overall maximum enstrophy.

(also shown in the rightmost portion of figure 12*c*), when the bundle of vortex lines is not twisted, the flexion line wraps around the vortex tube. With the twisting of the vortex tube (hence increasing the flexion product), the flexion lines are aligned in the direction of the vortex tube axis, as seen in figure 2(*b*) (also shown at the middle of figure 12*c*). Furthermore, core dynamics is inherent to coherent structures and vortex dynamics where non-uniform tube diameter along a vortex coils vortex lines which then propagate as waves along vortices. Such core dynamics, elucidated first and extensively studied by Melander & Hussain (1994), presumably can be useful in explaining the phenomenon of vortex bursting (E. Stout, personal communication).

Therefore, coiling and uncoiling of vortex lines in a twisted vortex tube represent one of the most dominant sources of aeroacoustic noise in vortex reconnection, i.e. flexion product term. As discussed above, being a purely hydrodynamic source term, the flexion product presumably plays a decisive role in the incompressible vortex reconnection. Furthermore, this term scales linearly with M_o (figure 11*a*); a detailed explanation of the role of compressibility in this term is outside the scope of the present work. To better understand the spatial distribution, we show the positive and negative isosurfaces of the flexion product along with the helicity density ($h = \boldsymbol{v} \cdot \boldsymbol{\omega}$) in figure 13; contours on the half of the bridge plane are also given. As in figure 12, these isosurfaces are for $M_o = 0.5$ at the time when the flexion product reaches its overall minimum. The large region of positive flexion product is predominantly caused by the typical alignment of the induced velocity and flexion vectors in a prototypical (or twisted) vortex tube. The negative flexion product
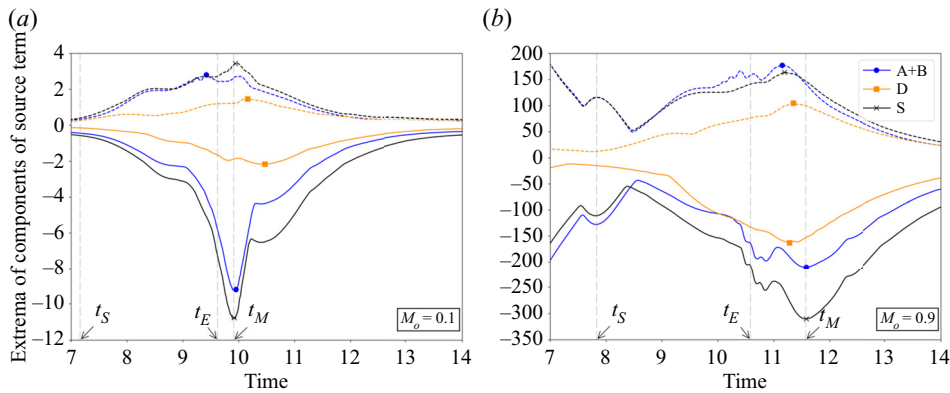
933 A34-16

Figure 14. Evolution of the minimum (solid line) and maximum (dashed line) of term A + B, term D and the source term at (a) $M_o = 0.1$ and (b) $M_o = 0.9$. Markers represent the overall extrema.

can only arise due to the coiling of twisted vortex tube; thus the negative isosurfaces of the flexion product are localized at specific points in and around the bridges (blue colour in figure 13a). The isosurface of helicity density (figure 13b) provides insight into the local alignment of the velocity and vorticity vectors at this specific time instant.

As depicted in figures 8 and 9, the amplification of the source term during reconnection is not as intense as those of its dominant components – which implies spatial cancellations between the source term's constituents. For instance, positive and negative contributions of the Laplacian of the kinetic energy neutralize the negative and positive contributions of the enstrophy and flexion product, respectively. Such mutual cancellation mechanisms have been observed in the sound generation in a mixing layer through vortex pairing (Colonius, Lele & Moin 1997; Cabana *et al.* 2008). Extrema evolution of the term A + B (the sum of terms A and B), term D and the source term is compared in figure 14. The amplification of A + B is less than that of its components, highlighting the cancellation between A and B. Another interesting point in figure 14 is the higher relative contribution of term D as M_o increases; compare figures 14(a) and 14(b). This conclusion could also be drawn by observing the linear and quadratic scalings of the source term and term D, respectively, in figures 7 and 11(d).

Let us explore the spatial distribution of the source term. Considering the moderate *Re* of the cases, the spatial evolution of the source term is nearly symmetric. As a result, we only present the contours on the half of the characteristic planes in the following figures. Figure 15 shows the source term contour on the collision plane at six times and for different M_o. The spatial distribution of the source term and the vorticity field evolution, visualized by the enstrophy line contour, remain essentially the same during the reconnection with subsonic initial conditions, although we note an intensification of the localized source term at higher M_o. Our results on the symmetric and bridge planes (not shown) also agree with this observation. Hereafter, we focus on the spatial distribution of the source term at $M_o = 0.5$, representing the general behaviour of the subsonic reconnection process at an average M_o.

The spatial distributions of the dominant components and the source term are compared on the collision, symmetric and bridge planes respectively in figures 16, 17 and 18. Positive regions of term A, which are primarily due to the flexion product (term A2 is negligible), nearly overlap the negative regions of term B. The same situation occurs for negative regions of term A, mainly originating from the enstrophy, and the positive regions of
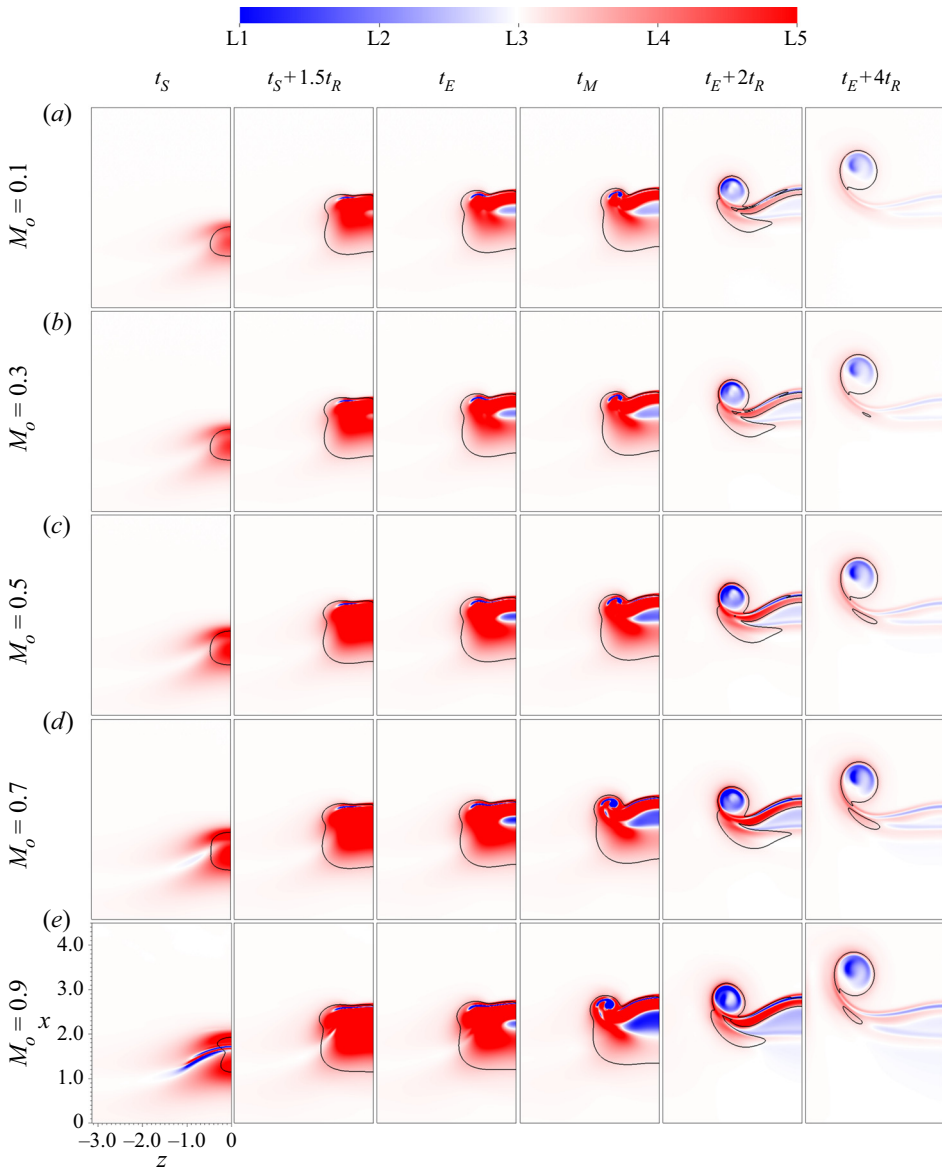
Figure 15. Source term contour on the collision plane. Limits of the global linear legend equal the negative and positive 5 % of the overall maximum absolute value of the source term. The solid line depicts the enstrophy contour set at 2 % of the overall maximum enstrophy.

term B. The importance of A over B is manifested by the qualitative resemblance between A and A + B. These contours also exhibit the inevitable role of term D which could be considered as a reinforcement of term A + B especially in the cores of the bridges and threads.

The flexion product is remarkably positive on the collision plane which implies high magnitudes of the velocity and flexion vectors and the acute angle between them. High-velocity plane jet on the collision plane is rooted in the induced velocity between the anti-parallel vortices. The high flexion magnitude on the collision plane originates
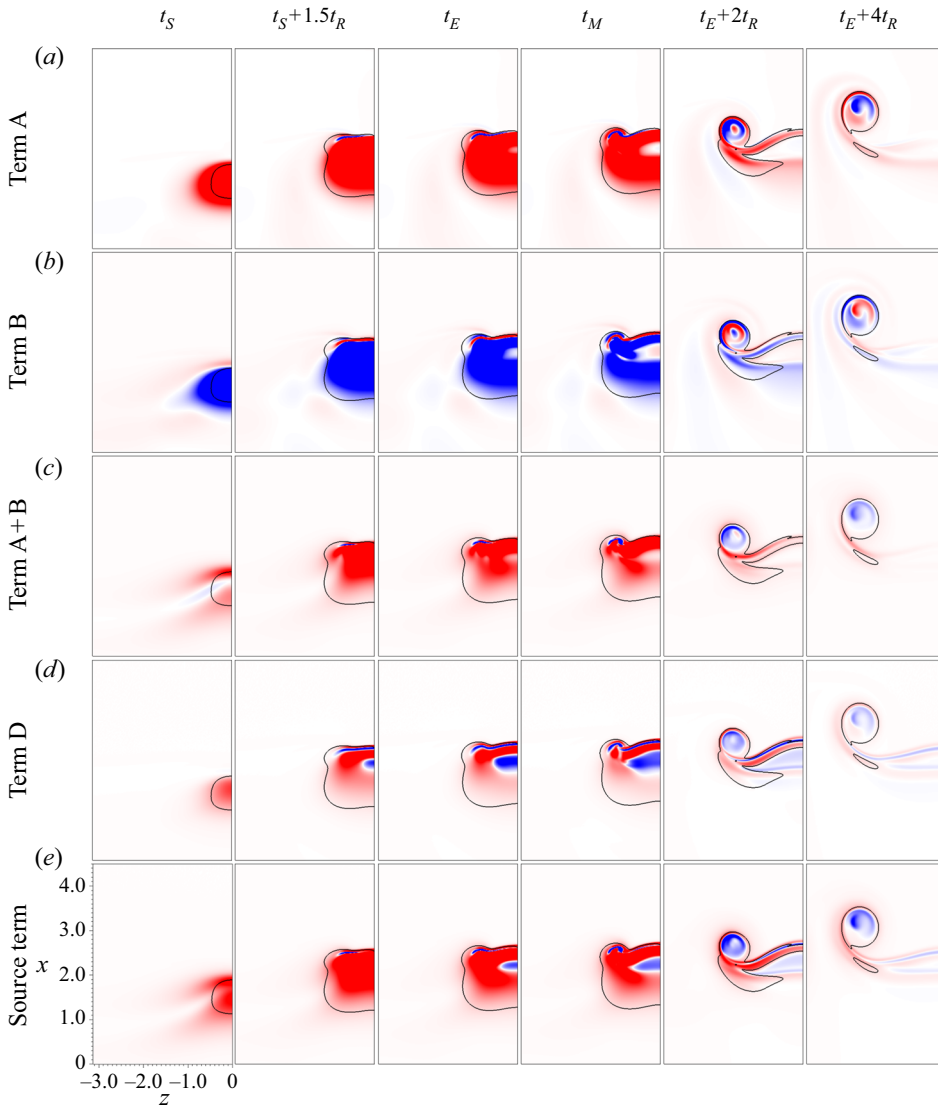
Figure 16. Source term contour and those of its dominant components on the collision plane at $M_o = 0.5$. The legend is the same as in figure 15.

from the rotation of the vorticity vector from the axial towards the lateral direction during reconnection. Indeed, the positive contribution of the flexion product is due to the acute angle between the velocity and flexion vectors. Further studies are required to characterize the evolution of these vectors in canonical vortical flows. Except at the vortex cores where the enstrophy is dominant, term A shows a positive contribution at other regions; see figures 16–18.

Considering the high velocity of the jet flow, the Laplacian of the kinetic energy, which is the dominant contributor to term B, becomes highly negative on the collision plane; see figure 16. The same explanation can be used around the vortex cores – because there is high velocity around the core of vortex. On the other hand, the low velocity gradient at the
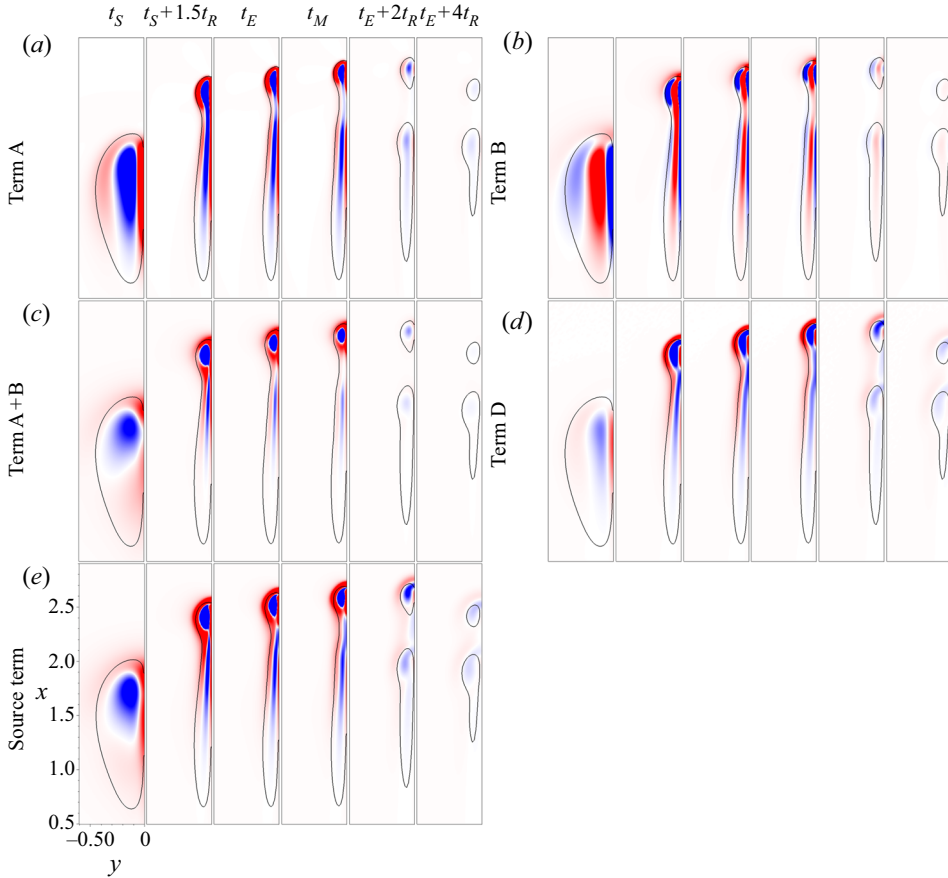
Figure 17. Source term contour and those of its dominant components on the symmetric plane at $M_o = 0.5$. The legend is the same as in figure 15.

vortex axis leads to positive values of term B; see figures 16–18. Thus, terms A and B are intense but mutually cancelling.

The deviation from the isentropic condition denotes a difference between the Laplacian of pressure and density while the latter has been multiplied by c_0^2; see (2.10). Where the pressure and density evolve isentropically, this term is exactly zero. Considering the equation of state and small temperature variations, the evolutions of pressure and density are similar. Low pressure and density in the vortex cores yield positive Laplacian in terms D1, $\nabla^2 P$, and D2, $-c_0^2 \nabla^2 \rho$. The results show that term D2 is dominant. Term D, identical to term A + B, becomes negative in the vortex cores, i.e. cores of bridges and threads; see figures 16–18. Note that the contribution of term D is more evident at the attachment of symmetric head–tail structures on the centreline, clearly shown by blue areas at the middle of the contours on the collision plane in figure 16. Despite similarities in the evolution as depicted in figure 19, the absolute minimum value of D2 is more than the maximum of D1, justifying the negative contribution of D in the vortex cores. Also, the relative effect of D2 including the Laplacian of density increases with M_o; compare the range of different terms in figure 19(*a,b*).

The evolution of the isosurface of the positive and negative source terms is presented in figure 20. At the start of reconnection, the negative source term is mainly located in the
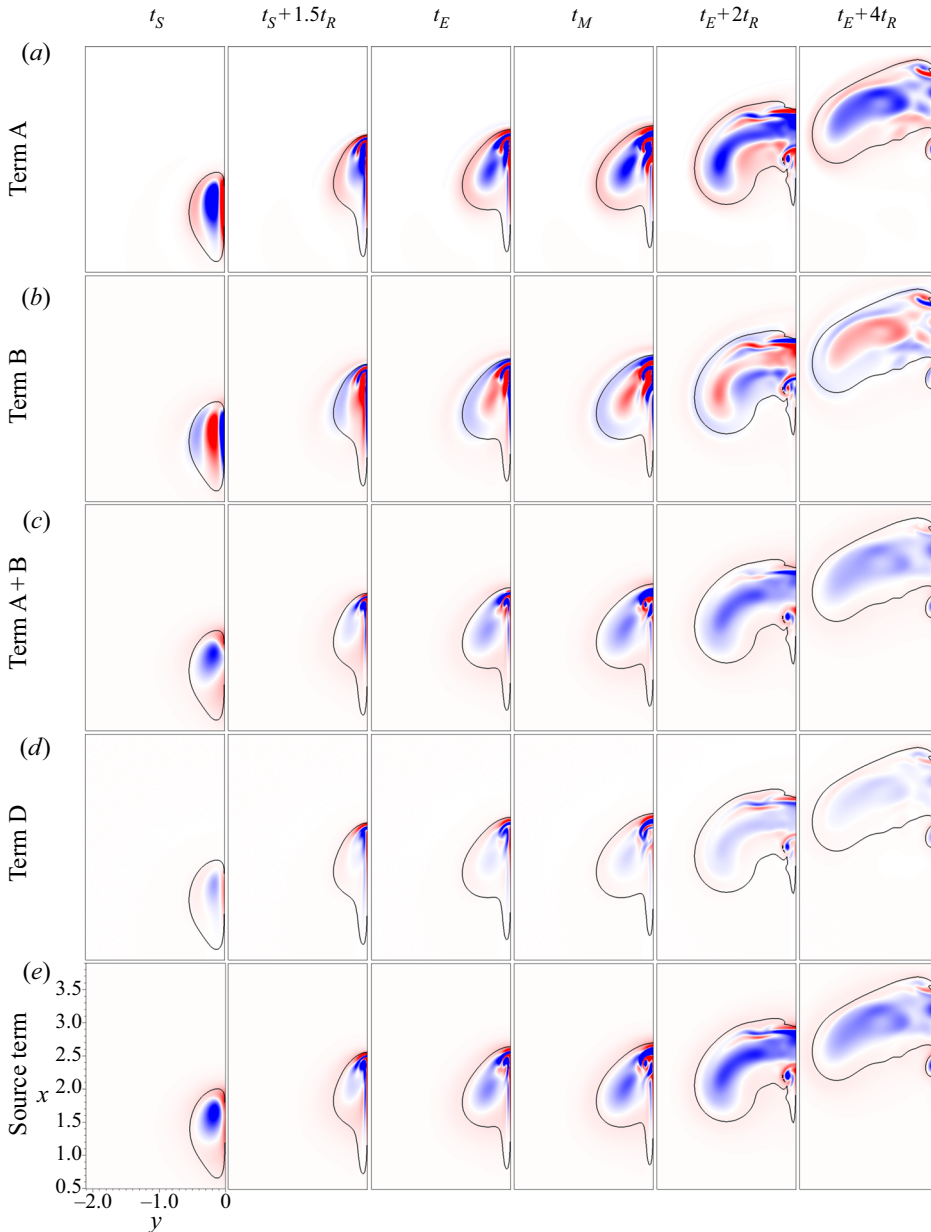
933 A34-20

Figure 18. Source term contour and those of its dominant components on the bridge plane at $M_o = 0.5$. The legend is the same as in figure 15.

vortex cores, while the positive part, due to the flexion product, extends on the collision plane and bends over the vortices. Halfway through the reconnection event, due to the deviation from the isentropic condition and the enstrophy term at the stretched tail of the well-known head–tail structure appearing as vortex sheets, the negative source term extends on both sides of the collision plane; compare figures 17 and 20(b) at $t_S + 1.5t_R$.

Because of the sign-changing characteristic of the Laplacian of pressure and density, a succession of negative and positive regions of term D is expected. Constructed by the
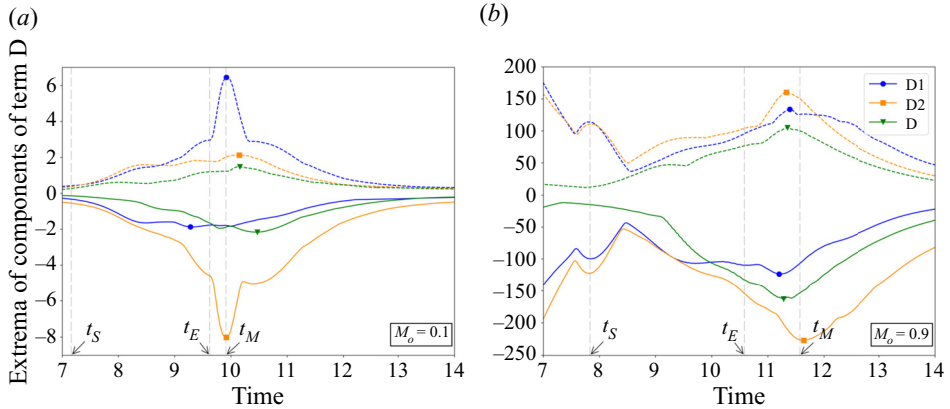
Figure 19. Evolution of the minimum (solid line) and maximum (dashed line) of terms D1, D2 and D at (*a*) $M_o = 0.1$ and (*b*) $M_o = 0.9$. Markers represent the overall extrema.
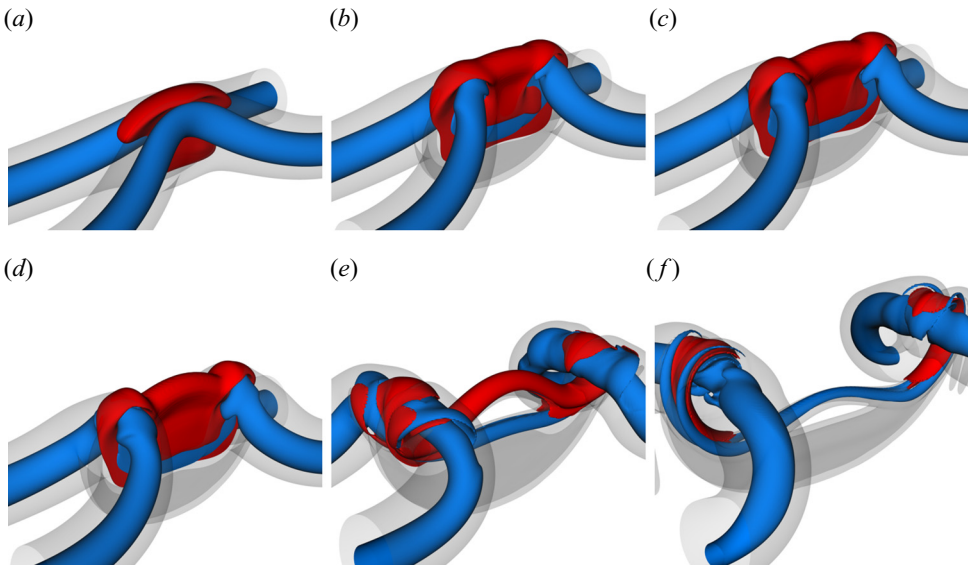

Figure 20. Source term isosurface of $M_o = 0.5$ at (*a*) t_S, (*b*) $t_S + 1.5t_R$, (*c*) t_E, (*d*) t_M, (*e*) $t_E + 2t_R$ and (*f*) $t_E + 4t_R$. Blue and red isosurface levels equal the negative and positive 1 % of the overall maximum absolute value of the source term. Grey transparent colour shows the enstrophy isosurface set at 2 % of the overall maximum enstrophy.

flexion product and the deviation from the isentropic condition, the positive isosurface of the source term emerges as parallel layers around the vortex sheets. Note that despite identical sheet-like structures, the red isosurfaces parallel to the collision plane do not represent regions of concentrated vorticity. Resorting to the same analysis, the development of the positive isosurface around the bridges and heads of the threads can be explained.

As time advances, vortex sheets extend in the axial and advection directions, as do positive layers of the source term; see figures 20(*c*) and 20(*d*). Once reconnection is complete and the bridges recoil from each other, entangled positive and negative source term isosurfaces are accumulated at bridges and threads while the cores of the vortices

933 A34-22

have negative contributions; see figures 20(*d*) and 20(*e*). Due to the global isosurface level used in figure 20, red positive layers may not be visualized enveloping the blue isosurfaces in vortex cores of the separated tails; however, a weak positive source term is still around the cores as demonstrated in the last two panels of figure 17. As stated earlier, the main positive source term is rooted in the flexion product and the angle between the velocity and the flexion vectors is critical in the sign of the contribution. The flexion vector evolution and its relation to the velocity vector in canonical vortical flows have not been studied yet.

4.2. *Near-field pressure evolution*

Consistent with the statements of Cabana *et al.* (2008), a non-zero source term – which is the essence of the sound production – is the result of subtle imbalances perturbing inherent spatiotemporal symmetry among components of the source term. However, the conversion mechanism of near-field energy into acoustic energy is not clear yet. It has been often acknowledged that the near-field pressure evolution could be critical in discerning the causality between the hydrodynamic effects and acoustic far-field pressure (Coiffet *et al.* 2006; Mancinelli *et al.* 2017). The pressure contour on the collision plane for different M_o is presented in figure 21. High pressure below the vortices can be observed at t_S. As time advances, vortex lines reconnect alongside the axial direction leading to the vorticity generation in the lateral direction; see the extended low-pressure region at $t_S + 1.5t_R$ and t_E showing the concentrated vorticity region in the lateral direction. Accumulation of the reconnected vortex lines in the bridges constructs the cores of reconnected vortex tubes manifested by dark blue colour at t_M. Note that, in addition to the twisted vortex line bundles (Virk *et al.* 1995), high pressure at the reconnection region could also affect the axial flow along the vortex core. Once the bridges are complete, the intensity of low core pressure decreases; see fading blue colour at $t_E + 2t_R$ and $t_E + 4t_R$.

Although the qualitative evolution is the same, spatial distribution of near-field low pressure is clearer at higher M_o; compare distribution of orange colour at low and high M_o in figure 21. More specifically, the rise of the near-field low pressure at t_E (Daryan *et al.* 2020), delimited by a dashed line, becomes more intense as M_o increases; follow the dashed line evolution at $M_o = 0.9$. Figure 22 shows the pressure contour on the symmetric plane. Although the low-pressure spatial distribution and sharp rise are obvious at higher M_o, the intensity of low pressure at the cores of threads always decreases as the lowest pressure is associated with the initial vortex tubes before reconnection. Low-pressure spatial distribution and sharp rise at higher M_o can be also seen in the near-field pressure evolution on the bridge plane; see figure 23. Owing to the repulsion of the bridges which reduces the high curvature of the reconnected, cusped vortex lines, the bridges extend in the lateral direction; see low-pressure extension at $t_E + 2t_R$.

The scaling of the overall extrema and maximum amplitude of pressure, which is normalized by γP_o, M_o is shown in figure 24. The overall extrema and the maximum amplitude of pressure follow a quadratic behaviour with M_o. In other words, not only the low-pressure spatial distribution, but also the pressure amplitude increases with M_o during reconnection. Note that at $M_o = 0.9$ the pressure amplitude is 92 % of the reference pressure. We do not expect this scaling to be maintained far into the supersonic regime.

4.3. *Far-field sound evolution*

Reconnection is a continuous process: anti-parallel vortex lines approach each other by self- and mutual induction, reconnect and recoil from each other by self-induction. Therefore, characteristic times are defined based on an integral quantity, i.e. circulation.
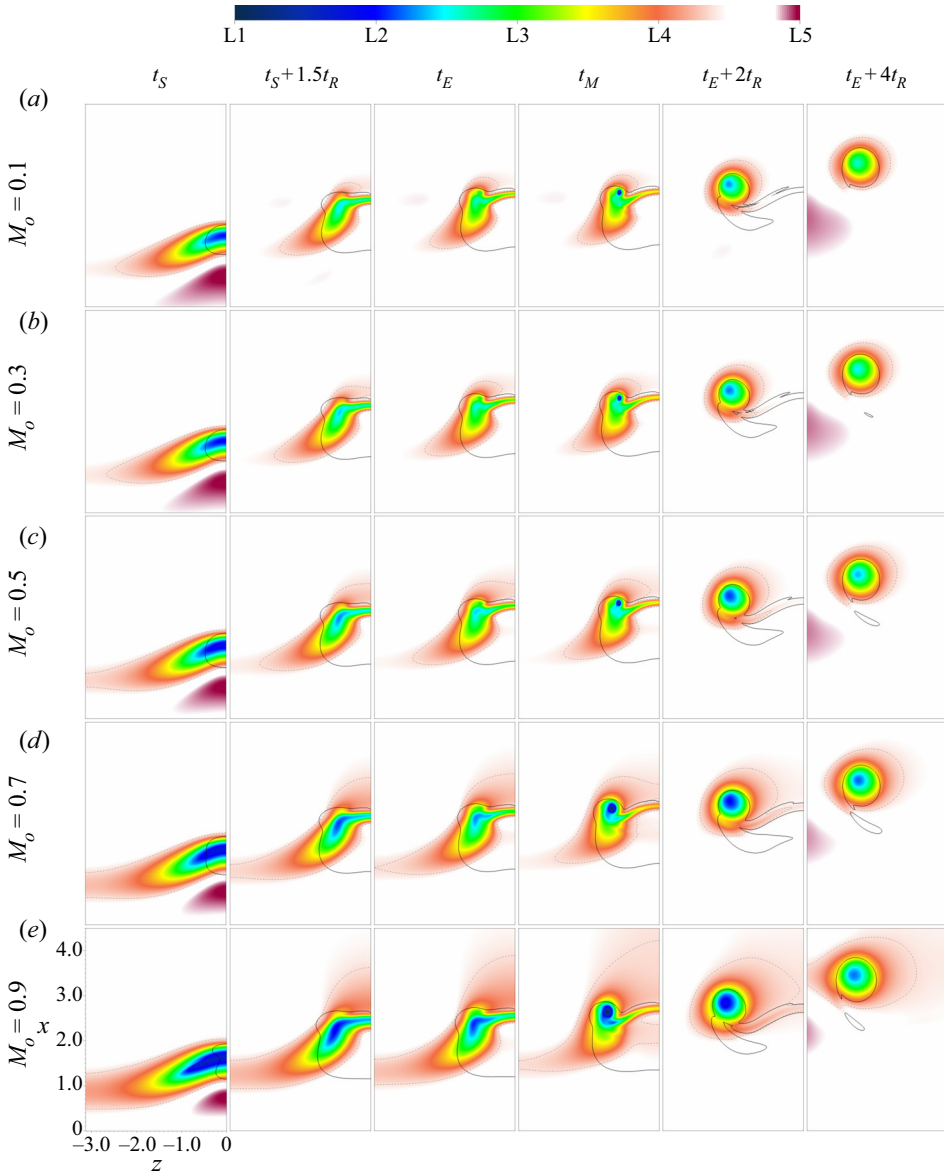
Figure 21. Pressure contours on the collision plane. Limits of the global linear legend equal the pressure overall extrema. The black solid line shows the enstrophy contour set at 2 % of the overall maximum enstrophy. The grey dashed line shows the pressure contour set at 84.5 % of the pressure range.

Assuming that reconnection of two anti-parallel vortex lines generates a sound pulse, we do not expect to capture a clear signal in the far field as reconnection occurs over a finite time and each vortex line reconnects at a slightly different stage during reconnection – some vortex lines are not yet reconnected while others are recoiling from each other. Localized acoustic source terms in the reconnection region could result in intermittent acoustic radiation (Scheidegger 1998). Although some clear instantaneous quadrupole patterns during reconnection of anti-parallel vortex tubes have been found (Daryan *et al.* 2020), we believe that reconnection of vortex filaments provides a more
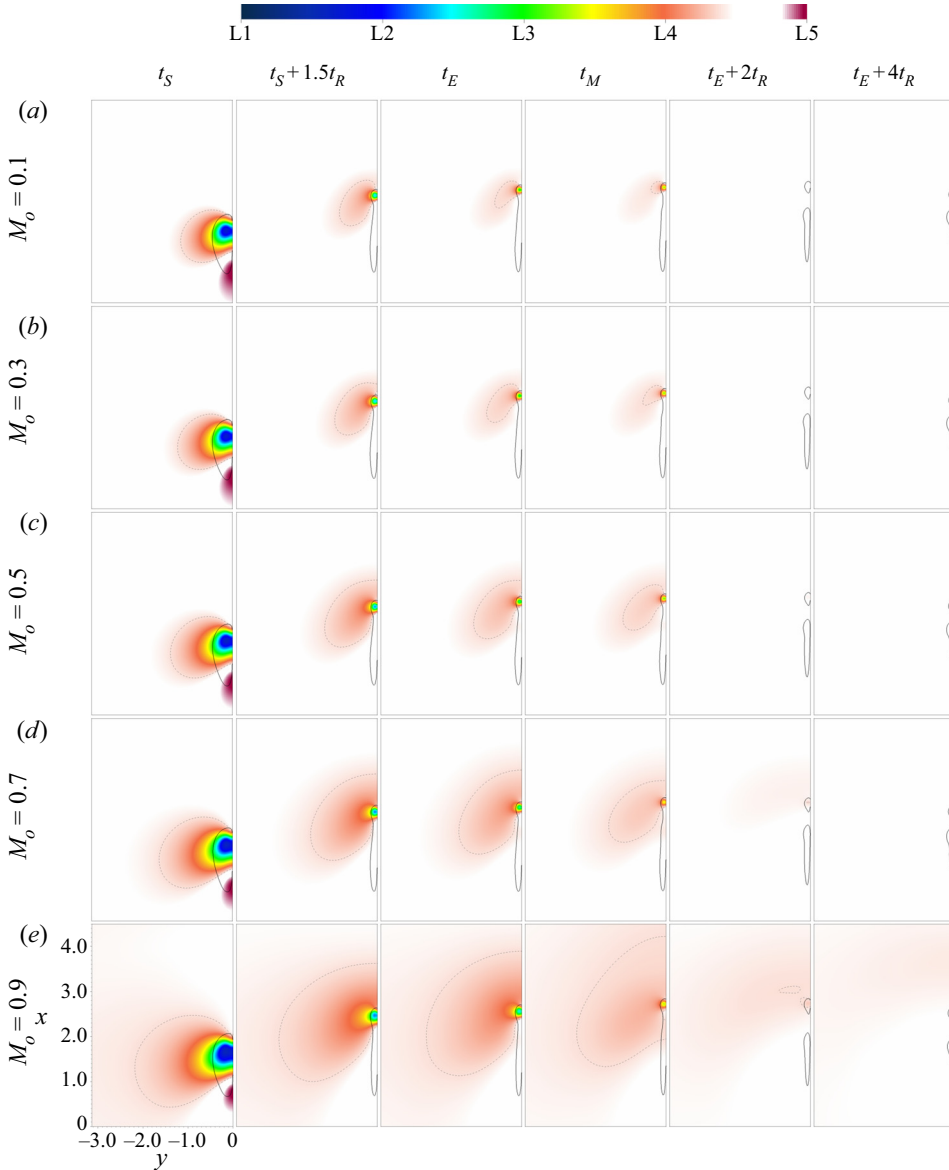
933 A34-24

Figure 22. Pressure contours on the symmetric plane. The description is the same as in figure 21.

exact sound pattern and scaling relations. Also, the comparison of the scaling relations of energy exchange in quantum reconnection could be a pivotal foundation in revealing complexities of the impulsive stochasticity and the dissipative feature of turbulent flows (Proment & Krstulovic 2020; Villois *et al.* 2020).

Figure 25 shows the maximum SPL evolution at different M_o on the symmetric and boundary planes. We assume that the sound source is located at the point with the maximum source term at each time. Then, the corresponding far-field sound is determined by considering a constant speed of sound, c_o; indeed, we offset the time of the far-field sound accordingly. Except for $M_o = 0.1$, a high level of far-field sound is captured during the time interval $t = [t_S, t_M]$. Note that the maximum sound does not necessarily occur
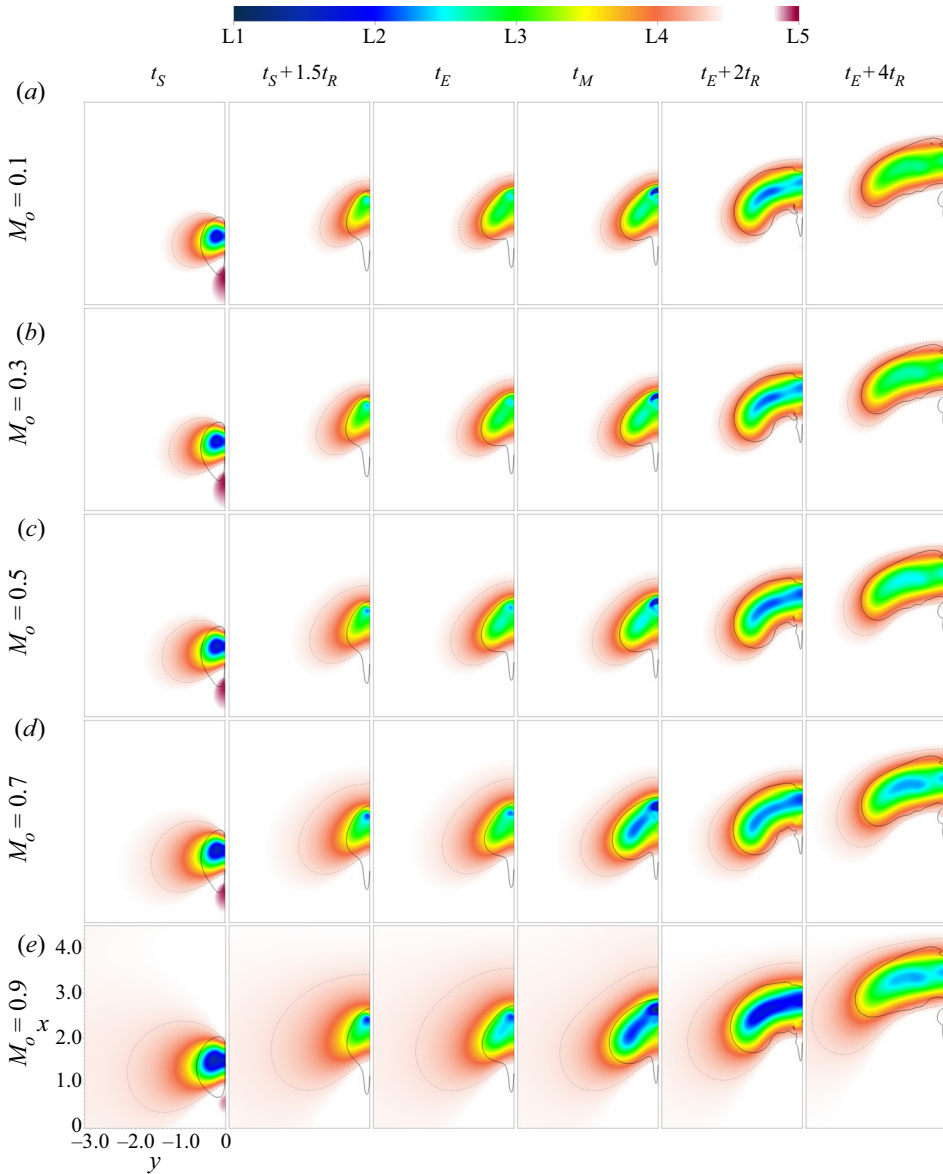
Figure 23. Pressure contours on the bridge plane. The description is the same as in figure 21.

at t_M, implying cancellation of acoustic waves is an important feature. As discussed, the finite time of the viscous reconnection process impedes the emergence of a clear sound pulse; however, the effect of reconnection on far-field sound level, especially at high M_o, can be observed.

Instantaneous sound directivity patterns of $M_o = 0.1, 0.5, 0.9$ at t_S and t_E are shown in figure 26. Although the quadrupole pattern is dominant, more complicated directivity patterns also appear during reconnection; see pattern of $M_o = 0.9$ at t_E on the boundary plane in figure 26(d). In our previous work (Daryan *et al.* 2020), the point with the maximum lateral vorticity is considered as the sound source location; therefore, the slight difference between the current results and previous instantaneous directivity patterns of
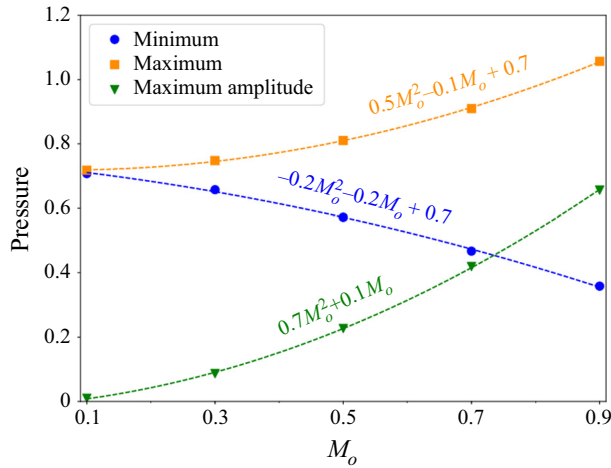
Figure 24. Scaling of the overall extrema and maximum amplitude of pressure.
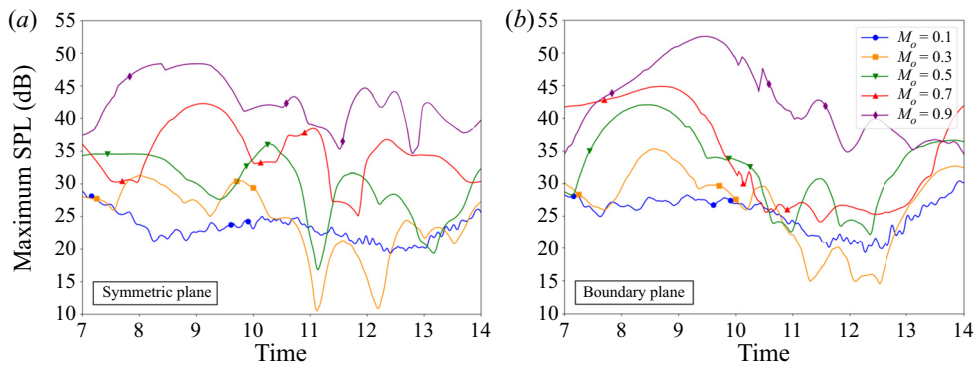

Figure 25. Maximum SPL evolution on the (*a*) symmetric and (*b*) boundary planes. Markers represent t_S, t_E and t_M.

$M_o = 0.5$ presented by Daryan *et al.* (2020) is acceptable. As another note, the increase in the SPL with M_o is clear in figure 26.

Figure 27 shows the time-averaged (taken over the time interval $[t_0, t_E + 4t_R]$) far-field sound directivity pattern on the symmetric and boundary planes. At low M_o, a quadrupole-like pattern can be observed. With an increase in M_o, not only does the sound level intensify, but the directivity pattern becomes elongated in the advection direction. Thus, compressibility plays a key role in the sound directivity of the reconnection process.

The scaling of the maximum instantaneous and time-averaged SPL on the symmetric and boundary planes is provided in figure 28. Despite the linear dependence of the maximum time-averaged SPL on M_o, instantaneous SPL follows a quadratic relation, consistent with near-field pressure scaling. There is a small change in the maximum instantaneous SPL for $M_o < 0.3$; see figure 28(*a*). Note that reconnection at $Re = 1500$ and $M_o = 0.9$ produces up to 52.7 dB far-field sound, reinforcing the claim that reconnection is one of the vortical interactions producing the most sound.
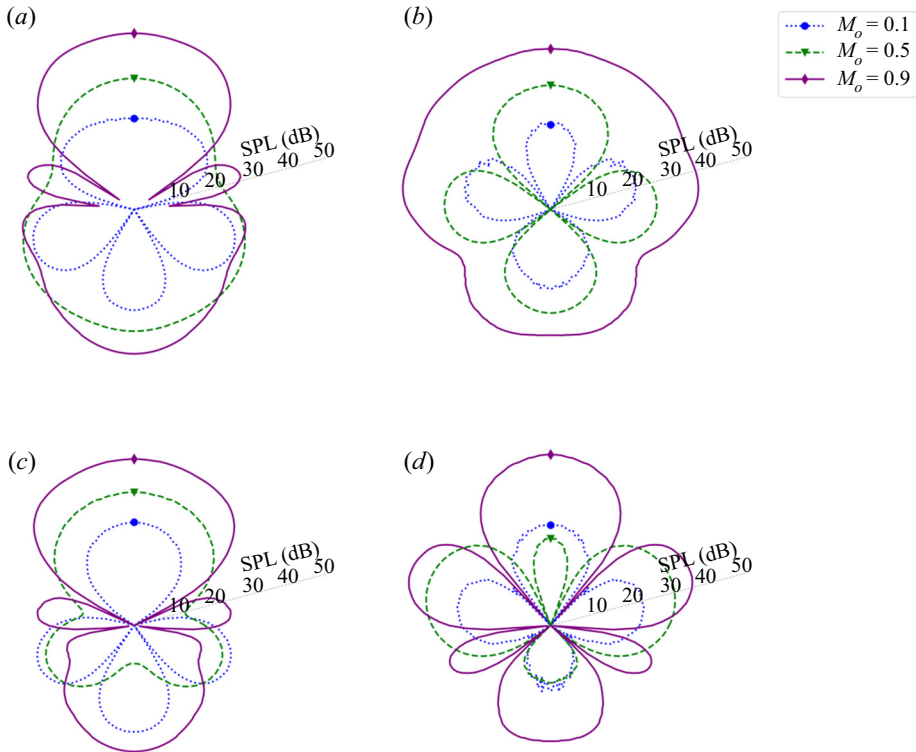
Figure 26. Instantaneous sound directivity pattern on the symmetric (*a,b*) and boundary (*c,d*) planes at (*a,c*) t_S and (*b,d*) t_E. Markers represent the advection direction.
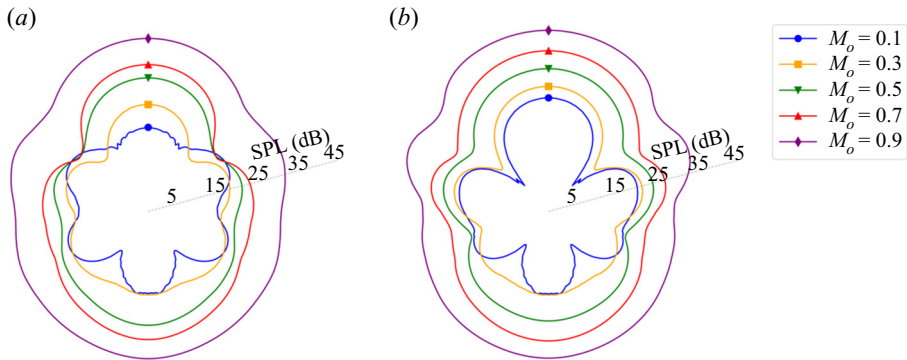

Figure 27. Time-averaged far-field sound directivity pattern of the reconnection process on the (*a*) symmetric and (*b*) boundary planes. Markers represent the advection direction.

5. Conclusion

We address the sound generation mechanism of viscous vortex reconnection via the analysis of the dominant components of Lighthill's source term. We study the initially subsonic, anti-parallel vortex pair reconnecting at $Re = 1500$ for reference Mach numbers of $M_o = 0.1$, 0.3, 0.5, 0.7 and 0.9. Although the time required for the circulation transfer is independent of compressibility, an increase of M_o postpones the onset of reconnection. Compressibility effects are the greatest initially at the entrained jet flow between the
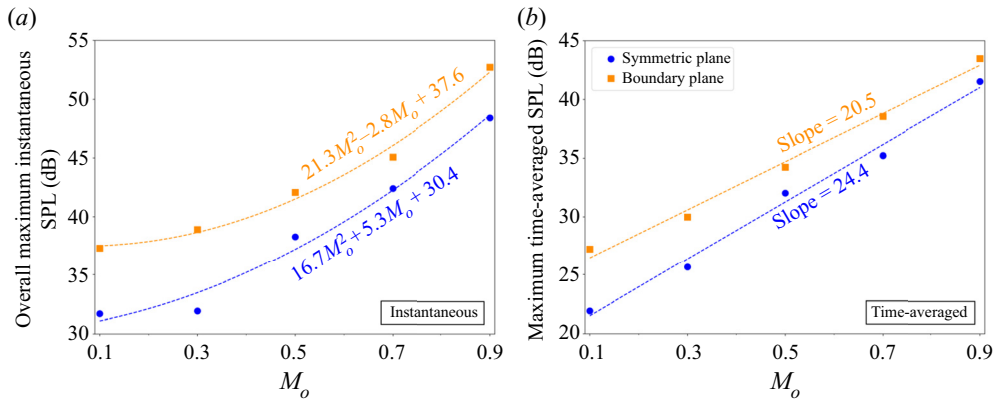
Figure 28. Scaling of (*a*) the overall maximum instantaneous SPL and (*b*) the maximum time-averaged SPL.

approaching vortices preceding reconnection. Soon after the start of reconnection, the regions of high local Mach number migrate towards the bridges. By considering only the time after the start of reconnection, t_S, the overall maximum local Mach number linearly scales as $M_{overall\,max} \approx 1.5M_o$.

The acoustic source strength is amplified during reconnection and emerges as a jump in the extrema evolution of the source term. Linear scaling of the overall extrema and maximum amplitude of the source term versus M_o manifests the direct effect of compressibility on the source term. To identify the dominant physical mechanisms of sound generation, the source term is decomposed into 14 physically meaningful terms and an order-of-magnitude analysis of each is performed. It is shown that dilatation effects and terms containing density gradient can be neglected in the absence of shocklets. Also, at the current Reynolds number, viscous effects do not contribute significantly to the acoustic source term. The Laplacian of the kinetic energy, flexion product, enstrophy, and deviation from the isentropic condition are found to be the dominant components of the source term. The first three, which are hydrodynamic, scale linearly with M_o; the departure from the isentropic condition follows a quadratic scaling, revealing the importance of the thermodynamic changes during reconnection at high M_o.

The flexion product is a hydrodynamic source term relating the velocity and flexion (curl of vorticity) vectors, and is intensified when these vectors are co-aligned. It is dominant when a twisted vortex tube undergoes a coiling or uncoiling motion. Physically, this arises as the pair of vortical threads are wrapped around the bridges after the end of reconnection, once a rapid strain is applied to the threads by the repulsion of the bridges. This purely hydrodynamic term scales linearly with the reference Mach number of the flow, suggesting an increasing importance of the hydrodynamically induced noise source as M_o increases.

The spatial distribution of the source term and the vorticity field evolution remain essentially the same during the reconnection at subsonic initial conditions. Exploring the spatial distribution, mutual cancellation of terms A and B becomes apparent (recall that the source terms are defined in (2.6)); unlike term B, term A is negative in vortex cores (due to the enstrophy term) and primarily positive at other regions (due to the flexion product term). Qualitative resemblance between terms A and A + B implies the importance of A over B in vorticity-concentrated regions. Term D (deviation from isentropic conditions) reinforces term A + B; ascendancy of term D2 ($-c_0^2 \nabla^2 \rho$) over D1 ($\nabla^2 P$) leads to the negative contribution of term D in the vortex cores at the bridges and threads.

933 A34-29

At the start of reconnection, the negative source term, due to the enstrophy term, is mainly located at the vortex cores, while the positive part, due to the flexion product, stretches on the collision plane in both axial and advection directions and also bends over the vortices. At later time, due to the deviation from isentropic condition and the enstrophy term at the stretched tail of the well-known head–tail structure appearing as vortex sheets, the negative source term extends on both sides of the collision plane. Once bridge formation is complete, entangled domains of positive and negative source term can be observed at bridges and threads.

Compressibility intensifies the spatial distribution and sharp rise of the near-field low pressure which fade away in time. Also, the overall extrema and the maximum amplitude of pressure are quadratically proportional to M_o. A high level of far-field sound is captured during the circulation transfer. At low M_o, the time-averaged sound directivity takes a quadrupole-like pattern. By increase of M_o, not only does the sound level intensify, but the directivity pattern becomes elongated in the advection direction. Consistent with the near-field pressure, the overall maximum instantaneous SPL follows a quadratic relation with M_o; however, the maximum time-averaged SPL shows a linear behaviour. Therefore, reconnection plays a key role in sound generation, especially as compressibility increases.

Author ORCIDs.

Ⓓ Hamid Daryan https://orcid.org/0000-0003-2803-4096;

Ⓓ Fazle Hussain https://orcid.org/0000-0002-2209-9270;

Ⓓ Jean-Pierre Hickey https://orcid.org/0000-0002-6944-3964.

REFERENCES

ADACHI, S., ISHH, K. & KAMBE, T. 1997 Vortex sound associated with vortexline reconnection in oblique collision of two vortex rings. *Z. Angew. Math. Mech.* **77** (9), 716–719.

BASTIN, F., LAFON, P. & CANDEL, S. 1997 Computation of jet mixing noise due to coherent structures: the plane jet case. *J. Fluid Mech.* **335**, 261–304.

BERMEJO-MORENO, I., BODART, J., LARSSON, J., BARNEY, B.M., NICHOLS, J.W. & JONES, S. 2013 Solving the compressible Navier–Stokes equations on up to 1.97 million cores and 4.1 trillion grid points. In *SC'13: Proceedings of the International Conference on High Performance Computing, Networking, Storage and Analysis*, pp. 1–10. IEEE.

BORATAV, O.N., PELZ, R.B. & ZABUSKY, N.J. 1992 Reconnection in orthogonally interacting vortex tubes: direct numerical simulations and quantifications. *Phys. Fluids* **4** (3), 581–605.

CABANA, M., FORTUNÉ, V. & JORDAN, P. 2008 Identifying the radiating core of Lighthill's source term. *Theor. Comput. Fluid Dyn.* **22** (2), 87–106.

COIFFET, F., JORDAN, P., DELVILLE, J., GERVAIS, Y. & RICAUD, F. 2006 Coherent structures in subsonic jets: a quasi-irrotational source mechanism? *Intl J. Aeroacoust.* **5** (1), 67–89.

COLONIUS, T., LELE, S.K. & MOIN, P. 1997 Sound generation in a mixing layer. *J. Fluid Mech.* **330**, 375–409.

CRIGHTON, D.G. 1981 Acoustics as a branch of fluid mechanics. *J. Fluid Mech.* **106**, 261–298.

CROW, S.C. 1970 Stability theory for a pair of trailing vortices. *AIAA J.* **8** (12), 2172–2179.

DARYAN, H.M.M., HUSSAIN, F. & HICKEY, J.-P. 2019 Aeroacoustic noise generation in compressible vortex reconnection. In *11th International Symposium on Turbulence and Shear Flow Phenomena, TSFP 2019*.

DARYAN, H., HUSSAIN, F. & HICKEY, J.-P. 2020 Aeroacoustic noise generation due to vortex reconnection. *Phys. Rev. Fluids* **5** (6), 062702.

DUCROS, F., LAPORTE, F., SOULÈRES, T., GUINOT, V., MOINAT, P. & CARUELLE, B. 2000 High-order fluxes for conservative skew-symmetric-like schemes in structured meshes: application to compressible flows. *J. Comput. Phys.* **161** (1), 114–139.

ELDREDGE, J.D. 2007 The dynamics and acoustics of viscous two-dimensional leapfrogging vortices. *J. Sound Vib.* **301** (1–2), 74–92.

GOLANSKI, F., FORTUNÉ, V. & LAMBALLAIS, E. 2005 Noise radiated by a non-isothermal, temporal mixing layer. *Theor. Comput. Fluid Dyn.* **19** (6), 391–416.

GUJ, G., CARLEY, M., CAMUSSI, R. & RAGNI, A. 2003 Acoustic identification of coherent structures in a turbulent jet. *J. Sound Vib.* **259** (5), 1037–1065.

HAMMAN, C.W., KLEWICKI, J.C. & KIRBY, R.M. 2008 On the lamb vector divergence in Navier–Stokes flows. *J. Fluid Mech.* **610**, 261–284.

HICKEY, J.-P., HUSSAIN, F. & WU, X. 2016 Compressibility effects on the structural evolution of transitional high-speed planar wakes. *J. Fluid Mech.* **796**, 5–39.

HUSSAIN, A.K.M.F. 1983 Coherent structures–reality and myth. *Phys. Fluids* **26** (10), 2816–2850.

HUSSAIN, A.K.M.F. & HASAN, M.A.Z. 1985 Turbulence suppression in free turbulent shear flows under controlled excitation. Part 2. Jet-noise reduction. *J. Fluid Mech.* **150**, 159–168.

HUSSAIN, A.K.M.F. & ZAMAN, K.B.M.Q. 1981 The preferred mode of the axisymmetric jet. *J. Fluid Mech.* **110**, 39–71.

HUSSAIN, F. & DURAISAMY, K. 2011 Mechanics of viscous vortex reconnection. *Phys. Fluids* **23** (2), 021701.

ISHII, K., ADACHI, S. & KAMBE, T. 1998 Sound generation in oblique collision of two vortex rings. *J. Phys. Soc. Japan* **67** (7), 2306–2314.

KAMBE, T., MINOTA, T. & TAKAOKA, M. 1993 Oblique collision of two vortex rings and its acoustic emission. *Phys. Rev.* E **48** (3), 1866.

KERR, R., VIRK, D. & HUSSAIN, F. 1989 Effects of incompressible and compressible vortex reconnection. *Topol. Fluid Mech.* 500–514.

KIBENS, V. 1980 Discrete noise spectrum generated by acoustically excited jet. *AIAA J.* **18** (4), 434–441.

KIDA, S. & TAKAOKA, M. 1987 Bridging in vortex reconnection. *Phys. Fluids* **30** (10), 2911–2914.

KIDA, S. & TAKAOKA, M. 1994 Vortex reconnection. *Annu. Rev. Fluid Mech.* **26** (1), 169–177.

KIDA, S., TAKAOKA, M. & HUSSAIN, F. 1991 Collision of two vortex rings. *J. Fluid Mech.* **230**, 583–646.

LARSSON, J., BERMEJO-MORENO, I. & LELE, S.K. 2013 Reynolds-and Mach-number effects in canonical shock–turbulence interaction. *J. Fluid Mech.* **717**, 293–321.

LAUFER, J. & YEN, T.-C. 1983 Noise generation by a low-Mach-number jet. *J. Fluid Mech.* **134**, 1–31.

LIGHTHILL, M.J. 1952 On sound generated aerodynamically I. General theory. *Proc. R. Soc. Lond.* A **211** (1107), 564–587.

MANCINELLI, M., PAGLIAROLI, T., DI MARCO, A., CAMUSSI, R. & CASTELAIN, T. 2017 Wavelet decomposition of hydrodynamic and acoustic pressures in the near field of the jet. *J. Fluid Mech.* **813**, 716–749.

MELANDER, M.V. & HUSSAIN, F. 1988 Cut-and-connect of two antiparallel vortex tubes. In *Studying Turbulence Using Numerical Simulation Databases, Proceedings of the 1988 Summer Program (Stanford University, Stanford, CA, 1988)*, pp. 257–286.

MELANDER, M.V. & HUSSAIN, F. 1994 Core dynamics on a vortex column. *Fluid Dyn. Res.* **13** (1), 1–37.

MÖHRING, W. 1978 On vortex sound at low mach number. *J. Fluid Mech.* **85** (4), 685–691.

NAKASHIMA, Y. 2008 Sound generation by head-on and oblique collisions of two vortex rings. *Phys. Fluids* **20** (5), 056102.

PANTANO, C. & SARKAR, S. 2002 A study of compressibility effects in the high-speed turbulent shear layer using direct simulation. *J. Fluid Mech.* **451**, 329–371.

PENG, N. & YANG, Y. 2018 Effects of the Mach number on the evolution of vortex-surface fields in compressible Taylor–Green flows. *Phys. Rev. Fluids* **3** (1), 013401.

POWELL, A. 1964 Theory of vortex sound. *J. Acoust. Soc. Am.* **36** (1), 177–195.

PROMENT, D. & KRSTULOVIC, G. 2020 Matching theory to characterize sound emission during vortex reconnection in quantum fluids. *Phys. Rev. Fluids* **5**, 104701.

SCHEIDEGGER, T.E. 1998 On compressibility effects in two-and three-dimensional flows: vortex dipoles and reconnection. PhD thesis, Rutgres University, New Brunswick, NJ.

SHIVAMOGGI, B.K. 2006 Vortex stretching and reconnection in a compressible fluid. *Eur. Phys. J. (B)* **49** (4), 483–490.

SIGGIA, E.D. 1985 Collapse and amplification of a vortex filament. *Phys. Fluids* **28** (3), 794–805.

TRETTEL, A. & LARSSON, J. 2016 Mean velocity scaling for compressible wall turbulence with heat transfer. *Phys. Fluids* **28** (2), 026102.

VILLOIS, A., PROMENT, D. & KRSTULOVIC, G. 2020 Irreversible dynamics of vortex reconnections in quantum fluids. *Phys. Rev. Lett.* **125**, 164501.

VIRK, D. & HUSSAIN, F. 1993 Influence of initial conditions on compressible vorticity dynamics. *Theor. Comput. Fluid Dyn.* **5** (6), 309–334.

VIRK, D., HUSSAIN, F. & KERR, R.M. 1995 Compressible vortex reconnection. *J. Fluid Mech.* **304**, 47–86.

WILLIAMS, J.E.F. & KEMPTON, A.J. 1978 The noise from the large-scale structure of a jet. *J. Fluid Mech.* **84** (4), 673–694.

YANG, D., GUZMÁN-IÑIGO, J. & MORGANS, A.S. 2020 Sound generation by entropy perturbations passing through a sudden flow expansion. *J. Fluid Mech.* **905**, R2.

YAO, J. & HUSSAIN, F. 2020 A physical model of turbulence cascade via vortex reconnection sequence and avalanche. *J. Fluid Mech.* **883**, A51.

ZAMAN, K.B.M.Q. 1985 Far-field noise of a subsonic jet under controlled excitation. *J. Fluid Mech.* **152**, 83–111.

ZAMAN, K.B.M.Q. & HUSSAIN, A.K.M.F. 1981 Turbulence suppression in free shear flows by controlled excitation. *J. Fluid Mech.* **103**, 133–159.